

Signatures of Gas Flows–II: Connecting the kinematics of the multiphase circumgalactic medium to galaxy rotation

Hasti Nateghi,^{1,2*} Glenn G. Kacprzak^{1,2}, Nikole M. Nielsen^{1,2,3}, Sameer^{4,5}, Michael T. Murphy¹, Christopher W. Churchill⁶, Jane C. Charlton⁵

¹Centre for Astrophysics and Supercomputing, Swinburne University of Technology, Hawthorn, Victoria 3122, Australia

²ARC Centre of Excellence for All Sky Astrophysics in 3 Dimensions (ASTRO 3D), Australia

³Homer L. Dodge Department of Physics and Astronomy, The University of Oklahoma, 440 W. Brooks St., Norman, OK 73019, USA

⁴Department of Physics and Astronomy, The University of Notre Dame, Notre Dame, IN 46544, USA

⁵Department of Astronomy and Astrophysics, The Pennsylvania State University, State College, PA 16801, USA

⁶Department of Astronomy, New Mexico State University, Las Cruces, NM 88003, USA

Accepted 2024 September 9. Received 2024 September 9; in original form 2023 November 3

ABSTRACT

The multiphase CGM hosts critical processes that affect galaxy evolution such as accretion and outflows. We searched for evidence of these phenomena by using the EW co-rotation fraction (f_{EWcorot}) to study the kinematic connection between the multiphase CGM and host galaxy rotation. We examined CGM absorption from HST/COS (including, but not limited to, Si II, C II, Si III, C III, and O VI) within $21 \leq D \leq 276$ kpc of 27 galaxies. We find the median f_{EWcorot} for all ions is consistent within errors and the f_{EWcorot} increases with increasing $N(\text{H I})$. The f_{EWcorot} of lower ionization gas decreases with increasing D/R_{vir} while O VI and H I are consistent with being flat. The f_{EWcorot} varies minimally as a function of azimuthal angle and is similar for all ions at a fixed azimuthal angle. The larger number of O VI detections enabled us to investigate where the majority of co-rotating gas is found. Highly co-rotating O VI primarily resides along the galaxies' major axis. Looking at the f_{EWcorot} as a function of ionization potential ($d(f_{\text{EWcorot}})/d(\text{eV})$), we find a stronger co-rotation signature for lower-ionization gas. There are suggestions of a connection between the CGM metallicity and major axis co-rotation where low-ionization gas with higher f_{EWcorot} exhibits lower metallicity and may trace large-scale filamentary inflows. Higher ionization gas with higher f_{EWcorot} exhibits higher metallicity and may instead trace co-planar recycled gas accretion. Our results stress the importance of comparing absorption originating from a range of ionization phases to differentiate between various gas flow scenarios.

Key words: galaxies: evolution – galaxies: haloes – quasars: absorption lines

1 INTRODUCTION

The CGM is a multiphase gaseous halo surrounding galaxies that hosts the baryon cycle which is primarily driven by accretion and outflows (Tumlinson et al. 2011, 2017). It holds significant reservoirs of neutral hydrogen and metals beyond the interstellar medium (ISM) of galaxies, extending outwards to the virial radius (e.g., Chen et al. 2010; Stocke et al. 2013; Tumlinson et al. 2017). Many studies have investigated the process in which gas travels through the CGM and approaches the disk to join the ISM to feed galaxy star formation. Hot and cold mode accretion are the best candidates for this process (e.g., Kereš et al. 2005, 2009; Dekel & Birnboim 2006; Faucher-Giguère & Kereš 2011a; van de Voort et al. 2011; Anglés-Alcázar et al. 2017; Strawn et al. 2021; Hafen et al. 2022; Afruni et al. 2023). Cold mode accretion dominates in lower mass ($\log(M_{\text{h}}/M_{\odot}) \lesssim 12$) galaxies, moving through the CGM as dense anisotropic filaments (Kereš et al. 2005; Dekel et al. 2009; Faucher-Giguère & Kereš 2011b; Stewart 2017), whereas the hot mode is more dominant in

massive halos ($\log(M_{\text{h}}/M_{\odot}) \gtrsim 12$) where the gas virializes to the temperature of the halo and infalls isotropically (Katz et al. 2003; van de Voort et al. 2011; van de Voort & Schaye 2012; Fielding et al. 2017; Hafen et al. 2022).

Cosmological simulations predict that the accretion of cold filaments occurs within an extended co-rotating disk aligned with the galaxy plane (Stewart et al. 2011a,b, 2013; Danovich et al. 2015; Nelson et al. 2016; Stewart et al. 2017; Suresh et al. 2019; Péroux et al. 2020). Connecting the kinematics of the CGM to the host galaxy rotation could then reveal signatures of gas flows. Utilising absorption lines present in the spectra of background quasars is still the best observational method to study the CGM and its kinematics. This approach enables us to unveil the multiphase gas in the CGM with different temperatures and densities, and to study their relative kinematics (e.g., Morris et al. 1993; Tripp et al. 1998; Kacprzak et al. 2008; Steidel et al. 2010; Rudie et al. 2012; Werk et al. 2014; Péroux et al. 2019; Nielsen et al. 2020; Nateghi et al. 2021). Indeed, the Cosmic Origins Spectrograph (COS) on *Hubble Space Telescope* (HST) enables us to detect numerous metal species, including C II, C III, C IV, Si II, Si III, Si IV, N V, and O VI, tracing low-, intermediate-,

* E-mail: hnateghi@swin.edu.au

and high ionization phases of the CGM. These absorption lines allow for an examination of the physical conditions and kinematics of the gas surrounding galaxies, especially in the low redshift Universe where galaxies are easy to identify.

The observational evidence for gas accretion is best found in studies of low ionization Mg II absorption along the major axes of galaxies that frequently reveal Doppler-shifted absorption with the same direction as the galaxy rotation (Steidel et al. 2002; Kacprzak et al. 2010; Bouché et al. 2013, 2016; Diamond-Stanic et al. 2016; Ho et al. 2017; Rahmani et al. 2018; Martin et al. 2019b; Lopez et al. 2020). This indicates that the low-ionization CGM most likely co-rotates with the galaxy disk even at substantial distances from the galaxy ($D \sim 100$ kpc), consistent with simulation predictions (e.g., Stewart et al. 2013). Using Λ CDM simulations Kacprzak et al. (2010) showed that the Mg II absorbing gas mostly originates from the filaments and tidal streams with inward velocities, falling into the host galaxies. Furthermore, Ho et al. (2019) used EAGLE simulations to indicate anisotropic accretion onto the galaxies where the gas is located within 10 deg and 60 kpc of the galaxy disk.

Given the multiphase nature of the CGM, the connection between the galaxies' rotational spin and the warm/hot halo is also important but less explored. From observations (e.g., Muzahid et al. 2015; Werk et al. 2016; Nielsen et al. 2017; Nateghi et al. 2021) and simulations (e.g., Churchill et al. 2015; Ford et al. 2014, 2016), we often expect different kinematics and absorption profiles for higher-ionization absorbers. Previous work has found that there was no strong correlation between the kinematic spread of gas and galaxy properties for the high ionization phase traced by O VI (Kacprzak et al. 2015; Nielsen et al. 2017; Kacprzak et al. 2019a; Ng et al. 2019). Nevertheless, Kacprzak et al. (2019a) found that there might be some observational connection between the kinematics of O VI absorption and galaxy rotation. They further used cosmological simulations to probe the kinematics of the gas which showed evidence of inflows along the major axis. However, they concluded that the observational kinematic signatures of O VI in accretion could be obscured by the broad distribution of the O VI velocities across the halo.

Studying H I kinematics (Barcons et al. 1995; Côté et al. 2005; French & Wakker 2020; Klimenko et al. 2023; Nateghi et al. 2024) may explain the disparity in the aforementioned studies and bridge the gap between the low- and high-ionization halos. Since the low-ionization phase of the CGM (Mg II) is mainly associated with strong H I absorption, while the high-ionization phase (O VI) is found for the entire H I column density range, the difference in co-rotation for Mg II and O VI would likely be reflected in weak and strong H I systems. Additionally, the absorption systems in the Mg II and O VI studies were categorised solely as either co-rotating or not based on whether the bulk of the absorption was consistent with the galaxy's rotation direction, without providing a quantification of the amount of gas in each system that could potentially co-rotate with the galaxy. As the O VI results suggest, there are likely many gas flows present along a given line-of-sight that could obscure accretion kinematic signatures.

In the first paper of this series, Nateghi et al. (2024, hereafter *GasFlows-I*), we addressed these shortcomings by studying a sample of 70 galaxy–quasar pairs that exhibit H I absorption with a large range of H I column densities ($12 < \log(N(\text{H I})/\text{cm}^{-2}) < 20$). We quantified the amount of gas that is consistent with galaxy rotation using the equivalent width co-rotation fraction, $f_{\text{EW,corot}}$. Our findings indicated a correlation between the co-rotation fraction of H I and its column density, which is consistent with the Mg II (high $N(\text{H I})$) and O VI (range of $N(\text{H I})$) results in the literature. We also found that the highest co-rotation fractions were located within the virial radius (R_{vir}) of galaxies, where metal lines are predominantly found,

although high co-rotation fractions were also found outside R_{vir} but only along the major axis (consistent with IGM accreting filament scenarios). Despite these results and the literature, it is still debated how the relative galaxy–CGM kinematics differs with ionization.

In this study, we aim to constrain the relative kinematics between the CGM and galaxies by investigating variations in CGM absorbing gas co-rotation across different ionization states. We use a subset of the *GasFlows-I* sample which has a range of low-, intermediate-, and high-ionization metal lines to characterise how the kinematics depend on ionization. The paper is organised as follows: In Section 2 we elaborate on the sample and our analysis. In Section 3 we present and explore the results of how $f_{\text{EW,corot}}$ varies as a function of the H I column density, impact parameter normalised to the virial radius, azimuthal angle, and ionization potential of different CGM species. We present our concluding remarks in Section 5. Throughout this paper, we adopt an $H_0 = 70 \text{ km s}^{-1} \text{ Mpc}^{-1}$, $\Omega_M = 0.3$, $\Omega_\Lambda = 0.7$ cosmology.

2 SAMPLE & METHOD

A sample of 27 galaxy–CGM metal absorption pairs ($0.09 < z < 0.5$, $z_{\text{median}} = 0.23 \pm 0.10$) is used to examine their kinematic connection in different ionization states. This is a subsample of the larger dataset consisting of 70 H I pairs examined in *GasFlows-I*. Each of the 27 galaxies studied here contains at least one detected metal-line detected in the spectrum of a single background quasar ($D = 21 - 276$ kpc; only one sightline per galaxy) observed with *HST/COS* and Keck/HIRES or VLT/UVES. Their H I column densities are shown as a function of impact parameter in Fig. 1 along with the distribution of halo masses. The galaxies have a halo mass range of $\log(M_h/M_\odot) = 10.5 - 12.3$ and their rotation curves were obtained with the Echelle Spectrograph and Imager (ESI, Sheinis et al. 2002) on Keck II as part of the analysis in *GasFlows-I*. Our sample contains both galaxy-selected (Pointon et al. 2019) and absorption-selected (Tripp et al. 2008) absorber–galaxy pairs.

Interactions in group environments or major mergers can complicate the kinematic connection between the galaxy and CGM. For example, there could be perturbations on the galaxy rotation curves or gas distributions due to interactions or major mergers. Because of this, our analysis primarily centres on isolated galaxies to minimise the influence of these external factors (*GasFlows-I*). Our galaxies were selected from (Pointon et al. 2019), who state that there are no major companions within 100 kpc or with velocity separations less than 500 km s^{-1} of their galaxies. The galaxies may still have nearby minor companions, which likely do not affect the kinematics of the larger galaxy.

Details regarding the metal lines observations and the galaxy sample can be found in Tables A1 and B1. We elaborate on the specifics of the data and analysis for this sample in the subsequent subsections.

2.1 Quasar Observations

2.1.1 Spectroscopy

HST/COS was used to obtain the UV spectra of background quasar in each field. The G130M and/or G160M spectra have a moderate resolving power of $R \sim 20,000$, giving a full width at half maximum of $\sim 18 \text{ km s}^{-1}$ and wavelength coverage of 1410–1780 Å. Further details regarding the QSOs spectroscopy and reductions are provided in Sameer et al. (in prep). In brief, the raw spectra were processed using the CALCOS V3.2.1 pipeline and then aligned and combined

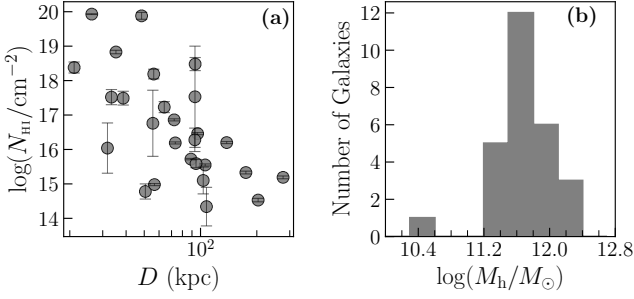


Figure 1. (a) Distribution of H I absorption column densities in our sample as a function of projected distance from galaxies. (b) The halo mass distribution of the galaxies in our sample.

following the method described in [Wakker et al. \(2015\)](#). The spectra are heliocentric corrected and have vacuum wavelength. When available, for 10/27 systems, we used Keck/HIRES or VLT/UVES quasar spectra to complement our *HST*/COS spectra by including Mg II absorption. The HIRES spectra were reduced using the Maunakea Echelle Extraction package or IRAF. The UVES spectra were reduced using the European Southern Observatory pipeline ([Dekker et al. 2000](#)) and the UVES Post-Pipeline Echelle Reduction (UVES POPLER) software ([Murphy et al. 2019](#)). All optical spectra have vacuum wavelengths and are heliocentric corrected.

Neutral hydrogen column densities are adopted from either [Sameer et al. \(2024\)](#), [Pointon et al. \(2019\)](#), [Tripp et al. \(2008\)](#) or *GasFlows-I* (see Table A1 in *GasFlows-I* for the references of the column densities) and range between $\log(N(\text{H I})/\text{cm}^{-2}) = 13.7 - 20$. Table A1 contains the H I column densities, which are also shown in Fig. 1.

2.1.2 Multiphase CGM Detections

We selected 27 galaxies from *GasFlows-I*, each hosting one or more of the following absorption lines: Mg II $\lambda 2796$, C II $\lambda 1334$, C III $\lambda 977$, C IV $\lambda 1548$, Si II $\lambda 1260$, Si III $\lambda 1206$, Si IV $\lambda 1393$, N II $\lambda 1083$, N III $\lambda 989$, N V $\lambda 1238$, and O VI $\lambda 1031$. It is important to note that not all ions are present in each system and Table B1 provides the detection information for individual galaxies. Among the detected transitions, Si II (16.3 eV, the ionization energy required to remove an electron from the neutral atom to create the ion), C II (24.4 eV), Si III (33.5 eV), C III (47.9 eV), and O VI (138.1 eV) had the highest detection rates, enabling us to perform statistical comparisons. Out of 27 systems, O VI was present in 25, Si III in 21, C III in 19, C II in 18 and Si II in 15. We also have 23 galaxies that host 3 or more metal-lines where we can further examine how the kinematics varies across different ions.

In Sections 3.2, 3.3, and 3.4, we analyse how the kinematics of CGM, traced by these ions, relate to H I strength, projected distances from the host galaxies, and orientation. In Section 3.5, we investigate how galaxy–CGM relative kinematics vary with ionization within individual systems, considering all of the aforementioned detected transitions. We explore whether these variations depend on galaxy orientation or CGM metallicity.

2.2 Galaxy Observations and Properties

2.2.1 Spectroscopy

The galaxy redshift zeropoints and their rotation curves are necessary to conduct this study of the galaxy–multiphase CGM relative

kinematics. We have observed the 27 galaxies discussed in this work using the Keck/ESI with a slit of $1''$ wide and $20''$ long. For each galaxy, the slit was aligned with the projected optical major axis of the galaxy to obtain the full range of rotation velocities as further explained in *GasFlows-I*. We used the standard echelle package in IRAF to combine the exposures and extract the spectra. The obtained echellette spectra have a wavelength coverage of $4000 - 11000 \text{ \AA}$ and are vacuum wavelength and heliocentric velocity corrected. Our ESI spectra have a spectral resolution of $R \sim 4600$ with a sampling rate of $22 \text{ km s}^{-1} \text{ pixel}^{-1}$ (FWHM $\sim 65 \text{ km s}^{-1}$).

We extracted the rotation curves of the galaxies using the same approach adopted by [Kacprzak et al. \(2010\)](#) which is similar to [Vogt et al. \(1996\)](#) and [Steidel et al. \(2010\)](#). In this method, we employed a three-pixel-wide aperture size and shifted it at one-pixel intervals along the spatial direction to extract a sequence of spectra along the major axis of each galaxy. Gaussian fits were conducted on the galaxy emission lines, primarily H α and H β , to obtain wavelength and line of sight velocity centroids. These centroids were then utilised to determine the systemic redshifts and rotation curves of the galaxies. The redshifts of the galaxies are presented in Table A1.

2.2.2 Imaging and Morphology

To establish a connection between the host galaxies and CGM absorption, we require information about the galaxy morphologies including inclination angles (i) and the orientation of the quasar sightline with respect to the galaxies’ disk (azimuthal angles, Φ). The $\Phi = 0$ and $\Phi = 90$ indicate the sightlines along the galaxies’ major and minor axes respectively. To measure these properties, we used images of each field having either ACS, WFC3, or WFPC2 on *HST* with the F702W, F814W, or F625W filters to model the galaxy morphologies/geometries (see Table B1 in *GasFlows-I* for imaging details). The inclination and azimuthal angles for each galaxy were modelled using the same method used in [Kacprzak et al. \(2011\)](#) and [Kacprzak et al. \(2015\)](#). In brief, this approach determined the orientation and morphological characteristics of galaxies by employing two-component models that include both a disk and a bulge. These models were implemented using the GIM2D software ([Simard et al. 2002](#)). The galaxies’ inclination and azimuthal angles are presented in Tables A1.

2.2.3 Mass and Virial Radius

We adopt the halo mass and virial radius of the galaxies from *GasFlows-I* where we convert the computed galaxy stellar masses (M_*) to halo masses (M_{h}) using the stellar-to-halo mass relation from [Girelli et al. \(2020\)](#). In summary, to compute the M_* for galaxies in this paper, we obtained Kron magnitudes in the g and r filters from Pan-STARRS ([Chambers et al. 2016](#)). We applied K -corrections following the procedures outlined in [Nielsen et al. \(2013\)](#) to derive the rest-frame absolute magnitudes in the g and r bands. For the 15 galaxies without observed $g - r$ colours, we made the assumption of an Sbc-type spectrum. The requirement that all of our galaxies have rotation curves derived from nebular emission lines means that they are emission line-selected and are therefore star-forming. This is consistent with the Sb-Sc type morphologies seen in the *HST* imaging of these galaxies, however we are unable to accurately classify them from these images alone. This choice also aligns with the typical coloration of galaxies associated with CGM absorption, as supported by previous studies ([Steidel et al. 1994](#); [Zibetti et al. 2007](#); [Nielsen et al. 2013](#); [Kacprzak et al. 2015](#)).

We calculated the stellar masses for all galaxies by employing the rest-frame $g - r$ colour and the g -band mass-to-light ratio (M/L) relation as described in [Bell et al. \(2003\)](#). We did not apply corrections for dust extinction since they are within the range of uncertainties associated with our method. We find good agreement with our stellar masses for 11 galaxies that overlap with the COS-Halos sample ([Werk et al. 2013](#)), yielding a mean difference of 0.065 dex between the two samples.

The galaxies' virial radii, R_{vir} , were determined using the methodology described in [Bryan & Norman \(1998\)](#). The halo masses and impact parameters normalised to the galaxies' virial radii (D/R_{vir}) can be found in [Table A1](#). The distribution of halo masses are also shown in [Fig 1](#).

2.3 Co-rotation Fractions

We employ the method developed in [GasFlows-I](#) to measure the absorption equivalent width (EW) co-rotation fraction. This method allows us to quantify the fraction of the absorption EW caused by the CGM gas that has velocities consistent with the rotation direction of the host galaxies. The advantage of this approach is that it relies more on the data itself rather than user-dependent absorption decomposition.

To first measure the total EW of each metal absorption line, we used the profile fits of the observed data, which were adopted from [Sameer et al. \(2024\)](#), in order to exclude any blends and obtain accurate profile boundaries. To fit the absorption profiles, they implement a multiphase Bayesian ionization modeling technique that operates on a cloud-by-cloud basis. This approach has been utilised to extract the physical properties of the absorption systems and shown to yield reliable measurements ([Sameer et al. 2021, 2022, 2024](#)).

For each galaxy, we then define a velocity window for its absorption lines, which includes all of the gas starting from the galaxy's systemic velocity to the edge of the absorption that resides in the direction of the rotation of the galaxy. We calculate the equivalent width in that window, which represents the absorption that aligns with the galaxy's spin direction along the quasar line of sight. We then divide that number by the total equivalent width of the absorption line and this quantity is referred to as the EW co-rotation fraction, f_{EWcorot} . A value of 1 indicates that all of the gas is consistent with a co-rotation scenario, while a value of 0 suggests that none of the gas is consistent with such a scenario. [Figure 2](#) in [GasFlows-I](#) describes this method. Typical errors on the co-rotation fraction were calculated by bootstrapping the errors associated with galaxy redshift and the absorption profile and range from 0.001 – 0.006.

3 RESULTS

We examine the kinematic relationship between galaxies and their surrounding multiphase CGM to quantify the fraction of gas that is consistent with possible co-rotation and/or accretion. In the following subsections, we explore the ions' co-rotation fractions, f_{EWcorot} , as a function of neutral hydrogen column density, impact parameter normalised to the virial radius, and azimuthal angle. We then examine how the co-rotation fraction of the CGM varies as a function of ionization and metallicity for galaxies that have at least three different CGM metal ions.

3.1 General statistics of co-rotation fractions

Observations of Mg II absorption found that the bulk of the gas is consistent with galaxy rotation (e.g., [Steidel et al. 2002](#); [Kacprzak et al. 2010](#); [Ho et al. 2017](#); [Zabl et al. 2019](#)), while observations of O VI show that only up to 50% of the gas can be co-rotating with the galaxy ([Kacprzak et al. 2019a](#)). In [Figure 2](#), we present the distribution of EW co-rotation fractions for a sample of ions. We find that there is a wide range of values ranging from 0 to 1 (see [Table C1](#)). We find that there is a skew toward unity, especially for Si II and C II and it seems to become more uniform for the higher ionization species. We further compute the median EW co-rotation fractions and the standard deviations for all of the systems, for a given ion, and find a value for Si II of 0.5 ± 0.4 , C II of 0.8 ± 0.3 , Si III of 0.5 ± 0.3 , C III of 0.7 ± 0.3 and O VI of 0.6 ± 0.3 . Note that while there is some variation in the median values, they are still consistent. However, not all ions are covered in each system so some system-to-system variations are expected. The fact that our EW co-rotation fractions are consistent between ions is also supported by previous observations showing that O VI exhibits similar, yet not identical, kinematics to H I and low-ionization absorption ([Tripp et al. 2008](#); [Werk et al. 2014](#)). [Martin et al. \(2019b\)](#) also provide an example where the strongest component of O VI has co-rotation consistent with Mg II absorption. We discuss how the co-rotation fraction of different ions varies for individual systems later in the Paper.

We also highlight that f_{EWcorot} values represent the statistical average of the fraction of the equivalent width that is consistent with being co-rotating with the galaxy for the population of galaxy-absorber pairs. For example, an average value $f_{\text{EWcorot}} = 0.5$ implies exactly half of the sample has most of their gas consistent with co-rotation and half inconsistent with co-rotation. This 50% should not be interpreted as random, but as the fraction of the sample that exhibits co-rotation. If we compare to the classical method (i.e., identifies which systems have the bulk of their absorption to the correct side of the galaxy rotation; [Steidel et al. 2002](#); [Kacprzak et al. 2010](#); [Ho et al. 2017](#)) we find 7/15 (45%) for Si II , 11/18 (61%) for C II , 11/21 (52%) for Si III , 11/19 (58%) for C III and 15/25 (60%) for O VI , which is consistent with the average EW co-rotation fractions reported above. Thus, our overall results are comparable to other studies using different methods to quantify kinematic coherency between galaxies and their absorption.

3.2 Co-rotation of CGM phases versus H I column density

[GasFlows-I](#) investigated the f_{EWcorot} of H I while examining its relationship with H I column density. They found a correlation between the H I column density and its co-rotation fraction where the co-rotation increased with H I column density. This is consistent with simulations suggesting that Lyman Limit Systems (LLSs) could effectively trace CGM gas dynamics, including processes such as accretion and outflows ([van de Voort et al. 2012](#); [Faucher-Giguère & Kereš 2011a](#); [Faucher-Giguère et al. 2015](#); [Hafen et al. 2017](#)).

Here we examine how the co-rotation fraction of different CGM ions is dependent on the H I column density. The top panel of [Figure 3](#) shows the first-order polynomial fit to f_{EWcorot} of each ion in relation to the H I column density ($\log(N(\text{H I})/\text{cm}^{-2})$). We tested higher order polynomial fits, but the first-order fit best represents the data. The 1σ error of the fits, represented by the shaded area, is determined by bootstrapping the fit and subsequently calculating the average and standard deviation across 10,000 realisations. Errors on all values are included in the bootstrapping here and in subsequent analysis. The absorbers are colour-coded according to their ionization potential.

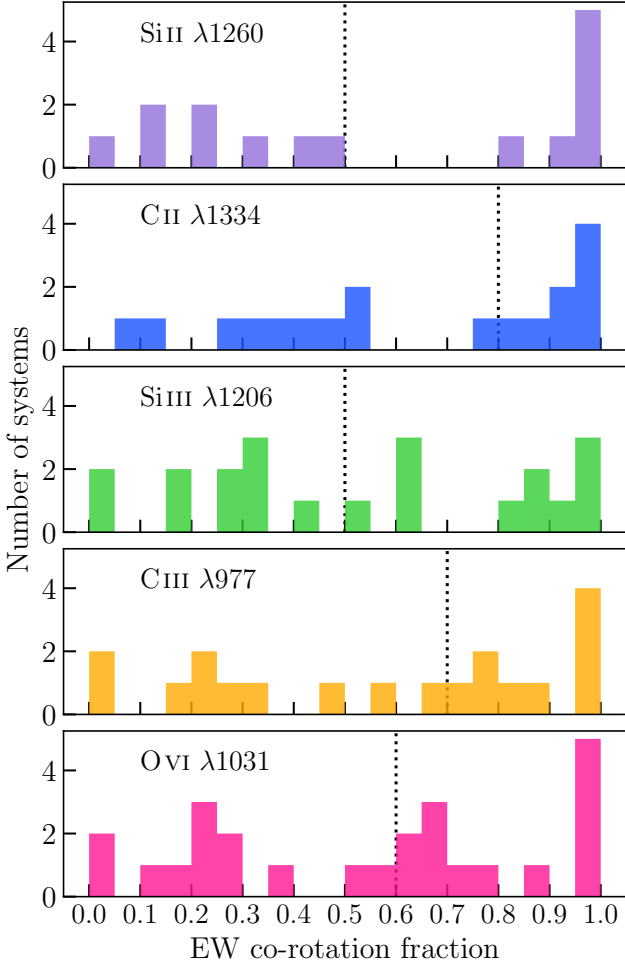


Figure 2. The co-rotation fraction distribution for our sample for a range of ions from the data listed in Table C1. Note that not all ions have the same number of systems (see text). The median is shown as a dotted black line. When the EW co-rotation fraction is greater than 0.5, we would consider that the bulk of the absorption is consistent with the rotation direction of the galaxy.

Cool colours represent ions from the low-ionization phase of the CGM, while warmer colours represent ions from the higher phases. The dark purple shows the $f_{EW\text{corot}}$ for the 70 H I absorbers from GasFlows-I, the light purple shows the fit to the 15 Si II absorbers, the blue shows the fit to the 18 C II absorbers, the green shows the fit to the 21 Si III absorbers, the yellow shows the fit to the 19 C III absorbers and the pink shows the fit to the 25 O VI absorbers. This figure shows the statistical average of the fraction of the equivalent width that is consistent with being co-rotating with the galaxy for the population of galaxy-absorber pairs.

We find that the co-rotation fractions of all ions are consistent within the errors with H I co-rotation fraction, which increases with higher H I column densities. The $f_{EW\text{corot}}$ for all the ions goes from ~ 0.4 to ~ 0.65 , for low to high column densities, respectively. To examine whether the $f_{EW\text{corot}}$ versus $N(\text{H I})$ varies with ionization, we explore the slopes of the fits to the $f_{EW\text{corot}}$ for each ion. In the bottom panel of Figure 3, the slope of the fit for each ion along with the corresponding 1σ bootstrap errors is presented. Overall within the errors, the slopes appear to be consistent. The data may hint that lower-ionization absorbers have a steeper slope, while higher-

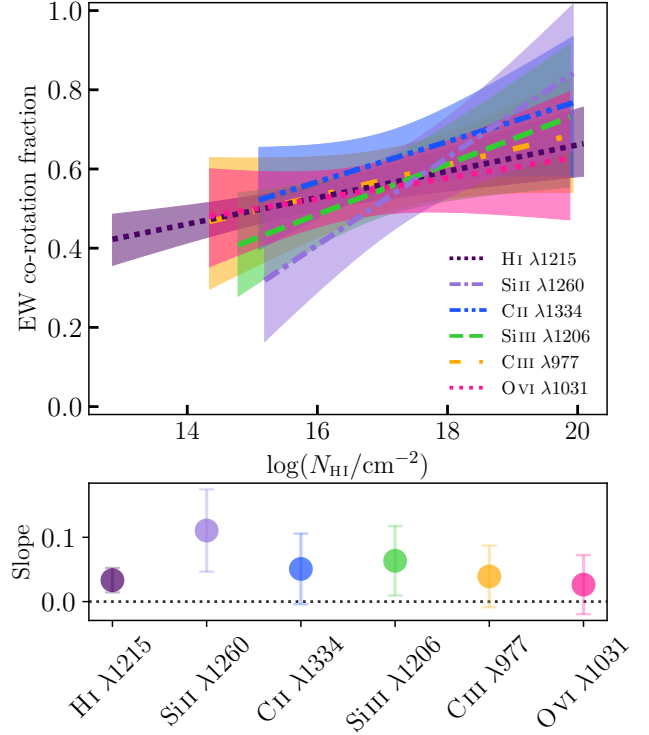


Figure 3. (top) The polynomial fit to equivalent width co-rotation fraction ($f_{EW\text{corot}}$) of H I and metal absorption lines as a function of H I column density. The ions are colour-coded, ranging from cool to warm colours corresponding to increasing ionization potentials. The shaded regions represent the 1σ bootstrap uncertainties on the fits. (bottom) The slope of the fit to each ion and 1σ bootstrap errors. The colour of the points corresponds to the respective ion and fits in the top panel. Overall within the errors, the slopes appear to be consistent for all ions.

ionization absorbers and H I have a more shallow slope, however we need more data to robustly determine this.

3.3 Co-rotation of CGM phases versus impact parameter

Although we expect an anti-correlation between the CGM absorption strength and impact parameter, D (e.g., Tumlinson et al. 2017), it is not clear how the co-rotation of metal absorbers behaves as a function of the galaxy–QSO projected separation. GasFlows-I investigated the $f_{EW\text{corot}}$ of the H I column density while examining its relationship with D/R_{vir} . They found a flat distribution of $f_{EW\text{corot}}$ for higher column density systems (that tend to reside within R_{vir}) as a function of D/R_{vir} . For low column density systems (that tend to reside beyond R_{vir}), $f_{EW\text{corot}}$ decreases with increasing D/R_{vir} .

Figure 4 (top) presents $f_{EW\text{corot}}$ as a function of impact parameter normalised to the virial radius (D/R_{vir}) for H I $\lambda 1215$ (dark purple), Si II $\lambda 1260$ (light purple), C II $\lambda 1334$ (blue), Si III $\lambda 1206$ (green), C III $\lambda 977$ (yellow), O VI $\lambda 1031$ (pink), which is sorted by ionization potential. The shaded regions around each fit represent the 1σ bootstrapped uncertainties. Since 25 out of the 27 metal-line systems presented here reside inside the virial radius (see Table A1), we focus on the variation of $f_{EW\text{corot}}$ within $1 R_{\text{vir}}$. The dark purple dotted line presents the fit to the 39 H I co-rotation fractions found within $1 R_{\text{vir}}$ from GasFlows-I for the purpose of direct comparison. On average, we observe a higher co-rotation in C II, Si II, Si III and C III lines closer to the galaxy, which tends to decrease with increasing

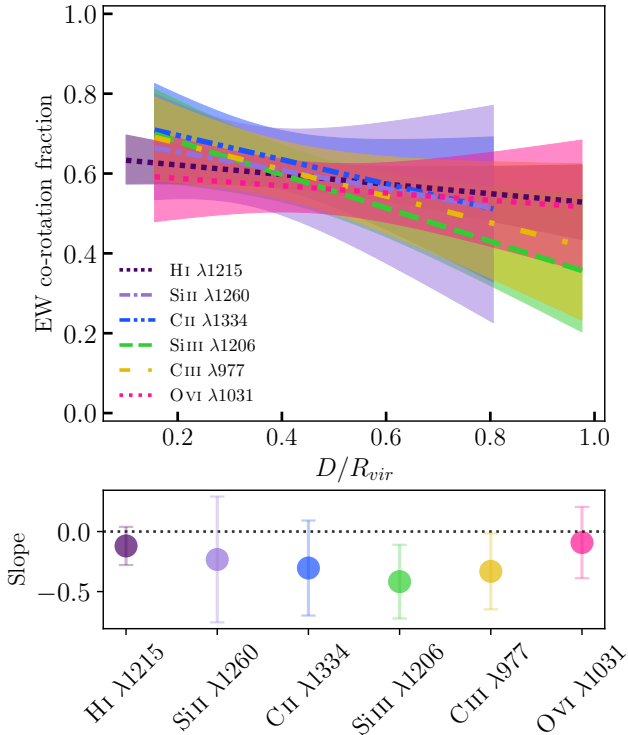


Figure 4. (top) The polynomial fits to equivalent width co-rotation fraction ($f_{EWcorot}$) as a function of D/R_{vir} . The ions are colour-coded from cold to warm colours with increasing ionization potentials. The shaded regions represent the 1σ bootstrap uncertainties on the fits. (bottom) The slope of the fit to each ion and 1σ bootstrap errors. The colour of the points corresponds to the respective ion and fits in the top panel.

D/R_{vir} . It appears that the O VI line is more constant across the full range of D/R_{vir} and the H I trend is in between that of the low and high ions. To examine this further we explore the slopes of the fits to the $f_{EWcorot}$ for each ion.

Figure 4 (bottom) shows the slope of the corresponding fit to $f_{EWcorot}$ versus D/R_{vir} and the vertical error bars represent the 68% confidence intervals obtained through bootstrapping. We find that all slopes are negative, but most are consistent with zero within uncertainties. We see hints that the slopes for the ions with lower ionization potential tend to be decreasing, while the ions with higher ionization potential (like O VI) have a flatter slope, however we need more data to robustly determine this.

3.4 Co-rotation of CGM phases vs azimuthal angle

Previous studies have shown that CGM gas exhibits a bimodality where the majority of the Mg II and O VI were detected along the galaxies' major and minor axes (e.g., Bordoloi et al. 2011; Bouché et al. 2012; Kacprzak et al. 2012; Kacprzak et al. 2015; Lan et al. 2014; Dutta et al. 2017; Lundgren et al. 2021). This is consistent with simulations where they depict the accretion of metal-poor gas along galaxies' major axis and enriched outflows perpendicular to the disk along the minor axis of the galaxies (Weiner et al. 2009; Nestor et al. 2011; Bouché et al. 2012; Kacprzak et al. 2014; Lan & Mo 2018; Schroetter et al. 2019). In GasFlows-I, the H I co-rotation fraction has a constant average value across all azimuthal angles within R_{vir} . However, beyond this region, it decreases by a factor of two for gas along the minor axis and for edge-on galaxies. This decrease along

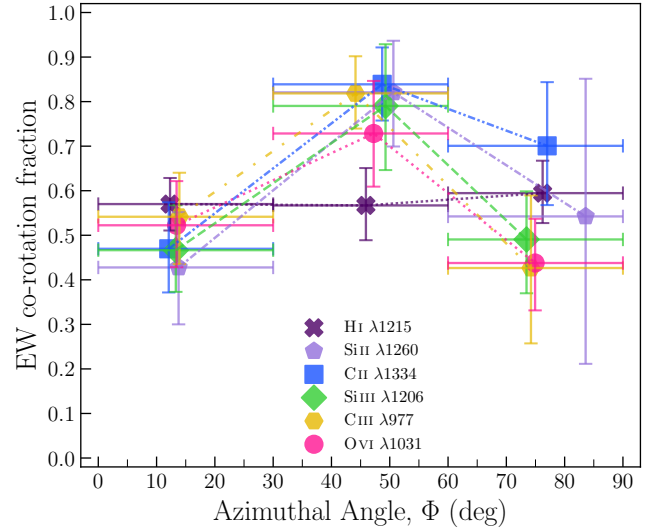


Figure 5. Average equivalent width co-rotation fraction ($f_{EWcorot}$) in 3 bins of azimuthal angles (Φ). The distinct shapes corresponding to different ions are the averaged $f_{EWcorot}$. The horizontal bars represent the azimuthal angles bins and the vertical error bars represent the 1σ bootstrapped errors on $f_{EWcorot}$. The co-rotation fractions of all ions are nearly consistent with H I within $1R_{vir}$, showing minimal variation across azimuthal angles with the errors, possibly peaking at the intermediate bin.

the minor axis was inferred to be due to outflows being bound to galaxy halos and not escaping. They further report that systems with significant co-rotation ($f_{EWcorot} > 0.5$) primarily exist along the major and minor axes of galaxies, where both inflows and outflows could have signatures of co-rotation.

Here we examine the connection between CGM gas flows in various ionization phases and their host galaxy orientations. Figure 5 presents $f_{EWcorot}$ as a function of azimuthal angle (Φ). Different point shapes represent the average $f_{EWcorot}$ in bins of Φ , with different ions indicated as follows: dark purple crosses for H I, light purple pentagons for Si II, blue squares for C II, green diamonds for Si III, yellow hexagons for C III, and pink circles for O VI. The horizontal bars present the azimuthal angles bins while the vertical bars present the 1σ bootstrap errors. For a fair comparison, we only plot 39 H I systems from GasFlows-I (purple distribution) detected within the virial radius of galaxies ($D/R_{vir} \leq 1$).

Similar to GasFlows-I, we find that the co-rotation fractions of all ions are roughly consistent with the H I as being nearly flat across all azimuthal angles with a possible peak at intermediate azimuthal angles. There is no variation between ions in each bin, within the errors shown here. Again, a larger sample may help to identify any possible differences if they exist. While this provides general statistics of the co-rotating gas as a function of azimuthal angle, what is more important is addressing where the co-rotating gas is primarily found.

To address where the majority of co-rotating gas is found, we computed the frequency of absorption systems as a function of the azimuthal angle. However, given the sample sizes, we are only able to perform this analysis using O VI, which has 15 galaxies hosting absorption with $f_{EWcorot} \geq 0.5$. We attempted this on other ions with no significant success as they have between 9–11 galaxies. Fig. 6 shows only O VI absorption systems that are dominated by co-rotating gas (e.g., the "bulk" of the gas where $f_{EWcorot} \geq 0.5$, which would be similar to other works). We adopt the methods of Kacprzak et al. (2012) and Kacprzak et al. (2015) to create asymmetric univariate

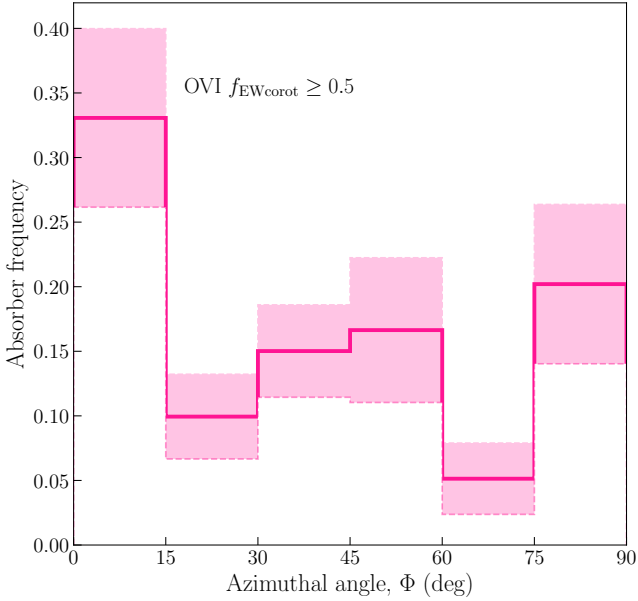


Figure 6. Distribution of OVI absorption systems that only have high co-rotation fractions ($f_{\text{EWcorot}} \geq 0.5$) with respect to azimuthal angle. The observed frequency in each 15-degree bin of Φ is shown with the solid pink line, with the 1σ error, measured by bootstrapping the sample, presented as the shaded region. Although we see a bimodality for the H I f_{EWcorot} (GasFlows-I), here we only find high co-rotation fractions along the major axis. We note that we do not have enough statistics to test this with other ions.

Gaussian PDFs (see Kato et al. 2002) using the measured galaxy azimuthal angles and their asymmetric uncertainties. This results in the mean PDF of all galaxies as a function of Φ , which represents the absorption frequency of co-rotating gas at a given Φ .

Fig. 6 shows the PDF, in 15 degree bins, for OVI where the bulk of the absorption is consistent with a co-rotation model. We find that there is a significant peak within 15 degrees along the major axis of galaxies, where accretion is expected to occur. With our current dataset, we do not find a peak along the minor axis. As a verification, we ensured that our sample of OVI absorbers has an azimuthal angle distribution consistent with being flat as expected for a random sample of galaxies. A Kolmogorov-Smirnov test shows that our sample is not discernible from a random population of galaxies within 1.3σ .

3.5 Co-rotation fraction as a function of ionization

Kinematic studies of the low-ionization CGM have found that Mg II absorption appears to be mostly consistent with the rotation of the host galaxies, while OVI shows that only about half of the higher ionization-phase CGM exhibits signatures of co-rotation. These results could imply a difference between the fraction of gas that is co-rotating with galaxies in different ionization states. In Sections 3.2 and 3.3, we found that the CGM co-rotation fractions as a function of H I column density and D/R_{vir} might be dependent on ionization.

One of the primary objectives of this study is to investigate how the CGM absorption co-rotation fraction varies as a function of ionization. To address this we examine the f_{EWcorot} of all the detected metals in each system, which is shown Figure 7. Each panel of Figure 7 is for a different galaxy with the name and redshift labelled on the top. Each panel shows the co-rotation fraction for each ion with measurable absorption, and for galaxies that have at least three

detected metal lines (23/27 galaxy–CGM pairs), with some galaxies having up to nine detected metal-lines. Their co-rotation fractions are shown as a function of ionization potential and the ions are colour-coded according to their ionization potential, with cooler colours representing the lower ionization species and warmer colours indicating the higher ionization species. The legend in each panel presents the colours and names corresponding to detected ions. The dashed line is a first order polynomial fit to the data, where we have measured the change in the EW co-rotation fraction as a function of ionization ($d(f_{\text{EWcorot}})/d(\text{eV})$) and 1σ errors.

From Figure 7, we identify that while each CGM ion has a range of co-rotation fractions, the co-rotation in individual systems also varies with ionization. In some cases, the range in f_{EWcorot} for an individual system can vary by as much as a factor of five (e.g., J100902+071343, $z_{\text{gal}} = 0.2279$) or show little variation at all (e.g., J104116+061016, $z_{\text{gal}} = 0.4422$), which indicates a wide distribution of the changes in the co-rotation fraction as a function of ionization ($d(f_{\text{EWcorot}})/d(\text{eV})$). The $d(f_{\text{EWcorot}})/d(\text{eV})$ in this distribution can also be positive or negative.

Figure 8 presents a histogram of $d(f_{\text{EWcorot}})/d(\text{eV})$ from Figure 7. The vertical green line shows the variance-weighted mean of the bootstrapped distribution while including their 1σ standard deviations in the re-sampling. The variance-weighted mean of $d(f_{\text{EWcorot}})/d(\text{eV}) = -0.00032 \pm 0.00001$, which indicates that we primarily find systems with negative $d(f_{\text{EWcorot}})/d(\text{eV})$. This histogram indicates that the majority of the systems ($16/23 = 70\%$), have higher co-rotation fractions in the low-ionization CGM compared to the high-ionization CGM.

To better quantify the co-rotation fraction of changes between different phases, Figure 8 also shows the difference between co-rotation fractions of the ion with the lowest ionization energy (Mg II) and the ion with the highest ionization energy (OVI), which is defined as $\Delta f_{\text{EWcorot}}(\text{Mg II} - \text{OVI})$. We do note that the Mg II and/or OVI were not detected in all of the systems as shown in Table B1. Thus we used $d(f_{\text{EWcorot}})/d(\text{eV})$ to compute the $\Delta f_{\text{EWcorot}}(\text{Mg II} - \text{OVI})$, which represents the maximum change in the co-rotation fraction for low to high ionization species. The $\Delta f_{\text{EWcorot}}(\text{Mg II} - \text{OVI})$ ranges between -0.4 and 0.4 , with most of the systems residing between 0 and -0.2 with a median value of -0.05 . This implies that while the majority of systems exhibit a higher co-rotation fraction for lower-ionization species compared to higher-ionization species, the difference can be small and suggests that there is significant kinematic consistency between ions.

In order to understand the origins of the different values of $d(f_{\text{EWcorot}})/d(\text{eV})$, we explored how they vary with galaxy properties such as halo mass, inclination and azimuthal angles, ISM and CGM metallicity, H I column density, and the impact parameter. Some trends might be expected given that ionization may change as a function of distance from the host galaxy, within outflows, or for different H I column densities. However, we did not find any significant connection between $d(f_{\text{EWcorot}})/d(\text{eV})$ and the aforementioned galaxy and/or gas properties with our current sample size. We do find a hint of a trend, which we describe in Figure 9. Figure 9 shows $d(f_{\text{EWcorot}})/d(\text{eV})$ as a function of azimuthal angle. Here we find that positive $d(f_{\text{EWcorot}})/d(\text{eV})$ values seem to reside around the major and minor axes of galaxies. Although this is only for a few systems, it is interesting that they do exist in those preferential locations.

Figure 9 also shows $d(f_{\text{EWcorot}})/d(\text{eV})$ as a function of azimuthal angles that are colour-coded with CGM metallicities ([Si/H] ratio). We adopted the CGM metallicities that were available for 20 systems in our sample from Pointon et al. (2019). To derive the CGM

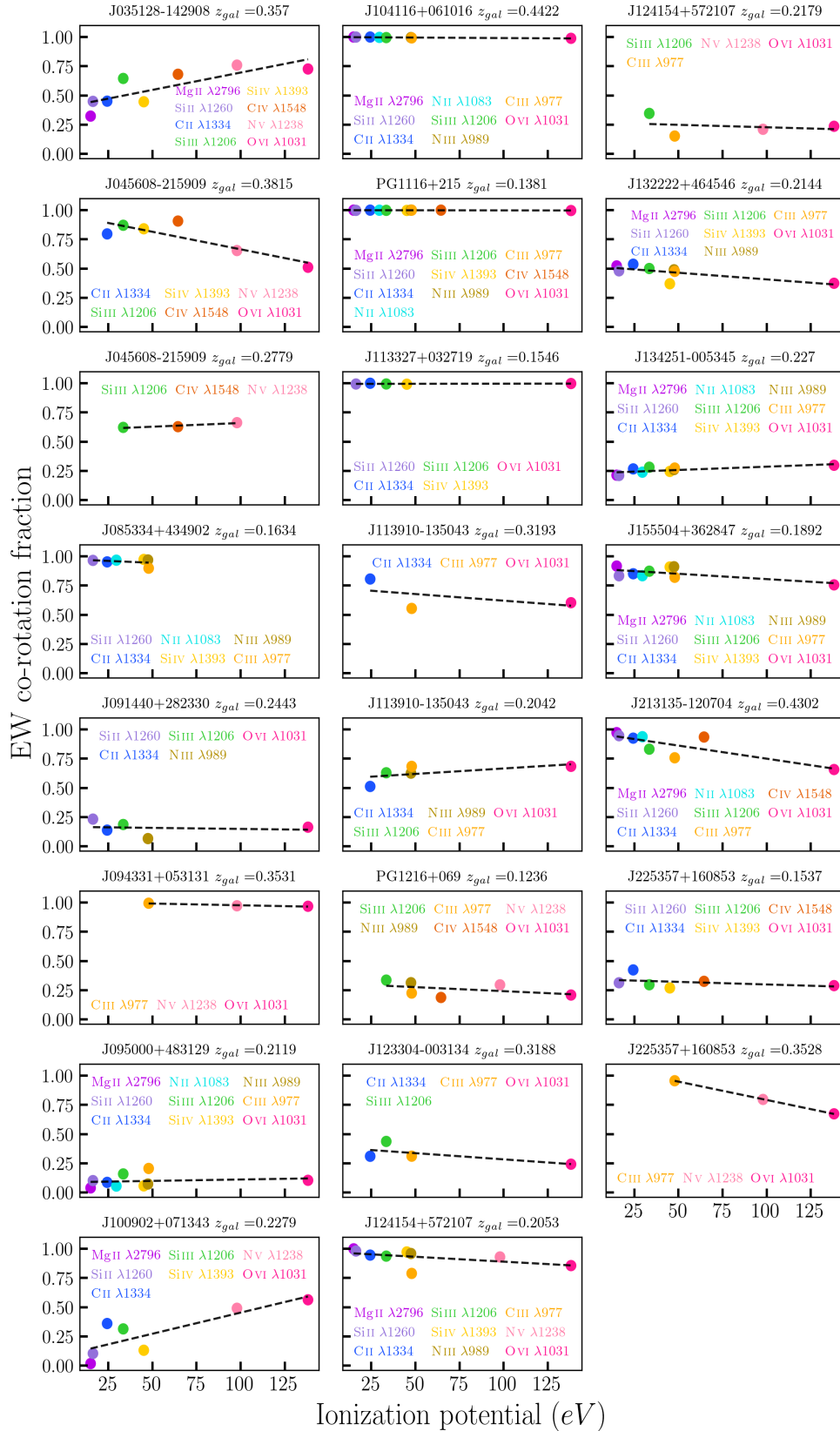


Figure 7. Metal absorption lines detected in each system with at least 3 ions and their EW co-rotation fractions ($f_{EW_{corot}}$) are displayed in each panel. Errors on $f_{EW_{corot}}$ are smaller than the points. The ions are colour-coded according to their ionization potential, with cooler colours representing the lower ionized species and warmer colours indicating the higher ionization states. The black dotted line presents the simple polynomial fit to the data points. The slope of the fit represents $d(f_{EW_{corot}})/d(eV)$, which is the change in the EW co-rotation fraction as a function of ionization potentials. The quasar field and galaxy redshift are labelled on top of each panel. The systems are arranged following the same order as Table A1 from the top left to the bottom right.

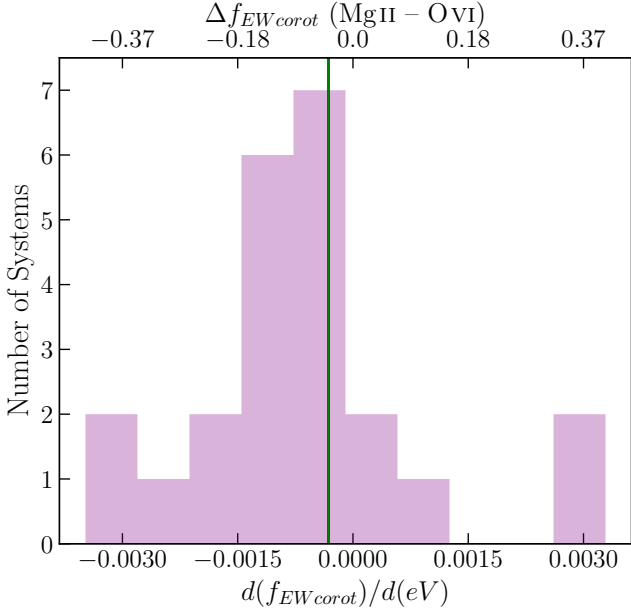


Figure 8. The distribution of the change in the co-rotation fraction as a function of ionization potential ($d(f_{EWcorot})/d(eV)$) for the fits to the EW co-rotation fractions as a function of ionization potential shown in Figure 7. The green line represents the average of the bootstrapped $d(f_{EWcorot})/d(eV) = -0.00032 \pm 0.00001$. This indicates that the majority of the systems exhibit negative $d(f_{EWcorot})/d(eV)$, implying that, on average, low-ionization gas has a higher co-rotation fraction compared to the higher-ionization phase. This is reflected in the top axis, which shows the computed difference between co-rotation fractions Mg II and O VI ($\Delta f_{EWcorot}(Mg II - O VI)$), which covers our full range of ionization potentials.

metallicities, Pointon et al. (2019) implemented the Cloudy ionization modelling software (Ferland et al. 2013) and the HM05 UV background (Haardt & Madau 1996) to generate grids of ionization properties and fit the grids. They employed the Markov Chain Monte Carlo (MCMC) technique, following the procedure described by Crighton et al. (2013), to ascertain the most probable metallicity, represented as the $[Si/H]$ ratio.

We find that within 20 degrees of the galaxies’ major axes, systems with smaller $d(f_{EWcorot})/d(eV)$ exhibit lower metallicity (darker purple), whereas systems with larger $d(f_{EWcorot})/d(eV)$ exhibit higher metallicity. Having fewer data points, we do see that for absorption along the minor axis ($\Phi \geq 60$ degrees), the opposite is true. In fact, systems with smaller $d(f_{EWcorot})/d(eV)$ exhibit higher metallicity (yellow), whereas systems with larger $d(f_{EWcorot})/d(eV)$ exhibit lower metallicity (darker purple). Overall, this may suggest a potential connection between gas accretion and CGM metallicity, particularly along the major and minor axes, where we expect gas accretion and outflows, respectively, to occur. We discuss this further in Section 4.

4 DISCUSSION

Studying how the CGM is kinematically coupled to its galaxy is critical in addressing how baryons are being processed. As the CGM is multiphase, it is unclear whether the different gas phases probe different baryon cycle processes. Here we investigate the galaxy–multiphase CGM kinematic connection primarily via Si II, C II, Si III,

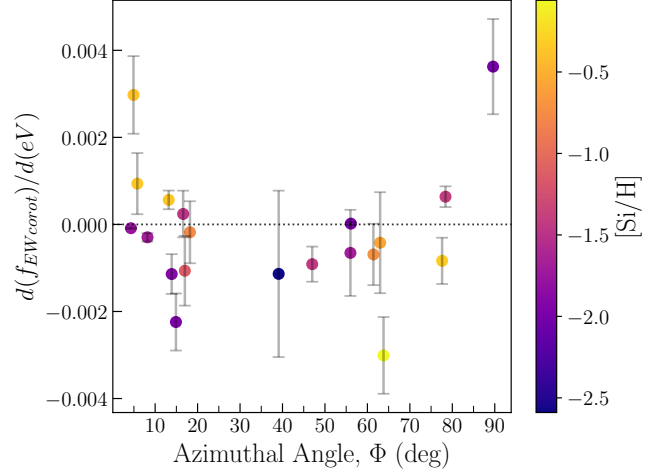


Figure 9. $d(f_{EWcorot})/d(eV)$ as a function of azimuthal angle. The vertical bars represent 1σ errors, and the data points are colour-coded based on the CGM metallicities adopted from (Pointon et al. 2019). We find that the majority of the systems have negative $d(f_{EWcorot})/d(eV)$, which implies that, on average, ions with lower ionization potential have higher co-rotation fractions compared to ions in higher CGM phases. Also, there are more systems with positive $d(f_{EWcorot})/d(eV)$ along the major and minor axes. This could imply that on average, higher ionization species have higher co-rotation fractions in these two preferential spatial projections. We further note that metallicity increases with increasing $d(f_{EWcorot})/d(eV)$ along the major axis, while the metallicity decreases with increasing $d(f_{EWcorot})/d(eV)$ along the minor axis.

C III and O VI to determine the statistical nature of how different phases are consistent with a co-rotation/accretion scenario.

4.1 $f_{EWcorot}$ dependence on $N(H I)$ and D/R_{vir}

Simulations show that the CGM gas with higher H I column density is more likely associated with accretion and outflows (Fumagalli et al. 2011; Suresh et al. 2019). From observations, Côté et al. (2005) found that the lower column density H I gas is likely connected to IGM filaments and with little-to-no co-rotation signatures. GasFlows-I also investigated the H I CGM kinematics with respect to the galaxy rotation and found a correlation between the H I column density and its co-rotation with the host galaxy. Our findings are consistent with previous studies and show that for systems associated with higher column density H I, low-ionization absorbers are more kinematically consistent with their host galaxies compared to high-ionization absorption. This could imply that low-ionization species are likely a better tracer of gas flows. However, given that $N(H I)$ is anti-correlated with galaxy–quasar projected separation (and references therein Kacprzak et al. 2021), it is important to address how the co-rotation fraction varies with the impact parameter.

French & Wakker (2020) reported a decrease in Ly α co-rotation fraction with increasing impact parameter. However, their sample mostly included absorbers with low column densities. GasFlows-I used a larger sample of H I absorption, with a wider range in column density, and normalised the impact parameters to the virial radius to account for the different halo masses and the self-similarity of the CGM (Churchill et al. 2013). Their results demonstrated a slight increase in the distribution of co-rotation fractions within the virial radius, particularly for high column density systems. However, beyond the virial radius, where lower column density systems dominate, co-rotation fractions decreased with increasing D/R_{vir} .

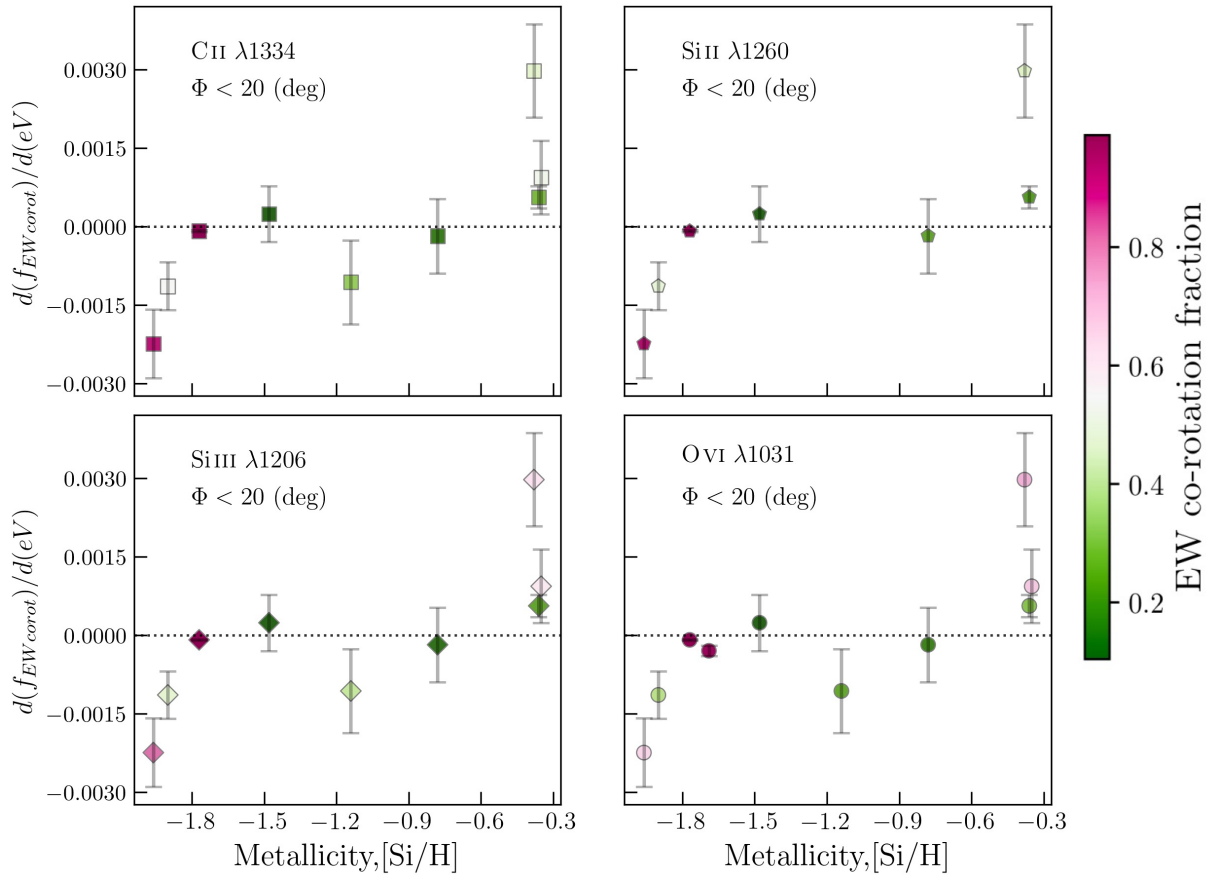


Figure 10. The change in the EW co-rotation fraction as a function of ionization ($d(f_{EW_{corot}})/d(eV)$) versus metallicity $[Si/H]$ for systems within 20 degree of the major axis. Points are colour-coded by EW co-rotation fraction of each ion. Comparing the four panels, we find that the major axis absorption with lower ionization energy and higher co-rotation fraction is associated with lower metallicities. While absorption with higher ionization energy shows high co-rotation fractions at the highest metallicities. This could be suggestive of two forms of accretion: 1) low ionization gas that is co-rotating with the galaxy having the lowest metallicity, which is accreting along cosmic filaments 2) high ionization and higher metallicity gas being recycled material that is cooling and joining with the accretion along the major axis. See Section 4.2 for further discussion.

Klimenko et al. (2023) presented a kinematics comparison between six galaxies and their H I+metal CGM absorption. They found agreement between the velocities of the strongest H I absorption components and the predicted radial velocities of the galactic disks. This occurs with 10 galaxy effective radii (~ 60 kpc), where absorption beyond this distance is mostly in the opposite direction to that expected from the galactic disk rotation. These results are consistent with a decreasing co-rotation fraction with increasing distance.

As shown in Section 3.2, our results suggest an anti-correlation between the EW co-rotation fraction of different ions and the D/R_{vir} . While the $f_{EW_{corot}}$ of species with lower ionization energy may gradually decrease with increasing D/R_{vir} , the $f_{EW_{corot}}$ of species with higher ionization energy remains almost constant across D/R_{vir} . Our findings indicated that closer to the galaxies, the low-ionization absorbers tend to have a higher EW co-rotation fraction compared to high-ionization absorption. This could provide further evidence for our expectation of low-ionization CGM being more associated with accretion scenario (e.g., Kacprzak et al. 2010; Ho et al. 2017; Martin et al. 2019a) compared to high-ionization CGM (Kacprzak et al. 2019a). This could also be consistent with the simulations of Oppenheimer (2018) who showed that for the hot gas, the tangential (line of sight) velocity versus D/R_{vir} trend is less steep than that of the cool gas. This could imply that the kinematics of the cool gas in CGM varies less significantly with the impact parameter normalized

by virial radius and the cool gas can likely be more coupled to the host galaxy.

It might be interesting to note that on average, the dependence of $f_{EW_{corot}}$ on D/R_{vir} is quite similar for all ions. This could imply that O VI is photoionized and remains so at all distances. This may differ from simulations that suggest we may find more photoionized O VI at only larger D/R_{vir} , especially at higher redshifts (Strawn et al. 2021).

Figure 4 and Figure 3 shows that for systems closer to galaxies (lower D/R_{vir}), or associated with higher H I column density, the average $f_{EW_{corot}}$ of H I appears to be in between the low and high ionization absorbers. This could be due to the H I contributing to both gas phases. Although, the slope of the EW co-rotation fraction versus $N(H I)$ is positive for all the ions, the trend for high-ionization absorption seems to be flat within the error. Thus for a further understanding of the change in the trends as a function of ionization, one would also have to consider how much H I is associated with each phase, i.e., O VI may only be associated with some fraction of the total H I (e.g., Muzahid et al. 2015; Sameer et al. 2021; Nateghi et al. 2021).

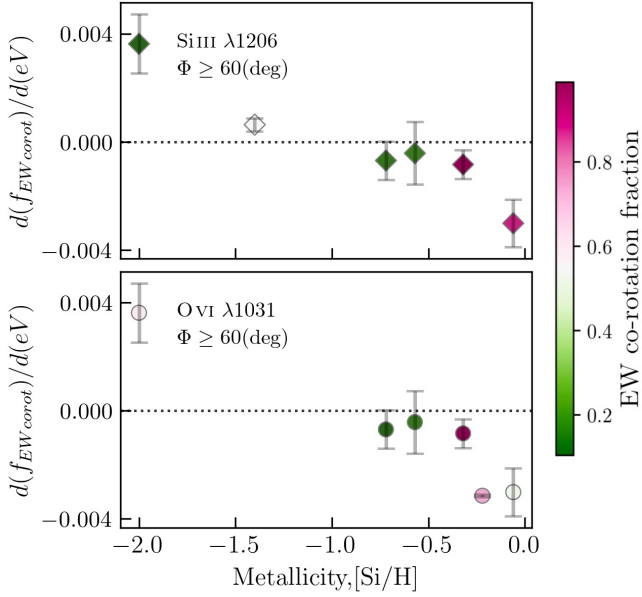


Figure 11. The change in the EW co-rotation fraction as a function of ionization potential ($d(f_{EWcorot})/d(eV)$) versus metallicity [Si/H] for systems with $\Phi \geq 60$ degree (along the minor axis). Points are colour coded by EW co-rotation fraction for Si III (top) and O VI (bottom). Minor axis absorbers, either with low or high ionization energy mostly exhibit negative $d(f_{EWcorot})/d(eV)$ values. Opposite to major axis absorption, systems with negative $d(f_{EWcorot})/d(eV)$ have higher metallicities. Systems with higher metallicity and also higher co-rotation fractions (white to pink shades) could potentially indicate metal-rich outflows that are still kinematically connected to the disk where they are ejected from. The minor axis systems, with low co-rotation fractions could be interpreted as the recycled gas that may become kinematically coupled and eventually accrete onto the galaxy.

4.2 $f_{EWcorot}$ dependence on Φ and metallicity

Previous observations have shown that the distribution of the CGM absorption is not uniform; instead, it exhibits a bimodality where the majority of the Mg II and O VI were detected along the galaxies’ major and minor axes (e.g., Bordoloi et al. 2011; Bouché et al. 2012; Kacprzak et al. 2012; Kacprzak et al. 2015; Lan et al. 2014; Dutta et al. 2017; Lundgren et al. 2021). This is consistent with simulations where they depict the accretion of metal-poor gas along galaxies’ disks and enriched outflows perpendicular to the disk and along the galaxy minor axis (Weiner et al. 2009; Nestor et al. 2011; Bouché et al. 2012; Kacprzak et al. 2014; Lan & Mo 2018; Schroetter et al. 2019).

We find that the co-rotation fractions of all ions are roughly consistent with the H I, remaining nearly flat across all azimuthal angles, with a potential peak at intermediate azimuthal angles. However, we next ask where gas resides that has the bulk (>50%) of the absorption consistent with co-rotation. While this could not be done with all ions, we find that the O VI residing along the major axis of galaxies tends to be co-rotating (Figure 6). This differs from GasFlows-I where they found that the H I has most of the co-rotating gas along the major and minor axes. It is unclear why this occurs as one would expect O VI to also occur in outflows, but maybe has little co-rotation signatures. It is possible that the low-ionization gas mimics the H I bimodality in the co-rotation fraction with azimuthal angle, however we are unable to test this with our current sample size. Although given that all metal ions seem to follow the same trend, it is not implausible that they exhibit a similar distribution to O VI; more studies are required here.

Despite this bimodal spatial distribution of the CGM, it is still debated how CGM metallicity varies with azimuthal angle. We might anticipate that gas with lower metal content would tend to accrete along the galaxy’s disk. Conversely, one would expect metal-enriched outflows to be more prevalent along the minor axis. This simple picture of the CGM is also consistent with predictions from simulations (e.g., Nelson et al. 2019; Péroux et al. 2020; Weng et al. 2023). Yet observations of CGM metallicity (Péroux et al. 2016; Pointon et al. 2019; Kacprzak et al. 2019b; Sameer et al. 2024) do not reveal a dependence on geometry. However, when dust is accounted for in the metallicity calculation, it was determined that lower metallicity can be found along the major axis and a higher metallicity along the minor axis of galaxies (Wendt et al. 2021).

Although our results do not imply a significant relation between the $f_{EWcorot}$ of different ions and their azimuthal distributions, there are some hints of a connection between the $f_{EWcorot}$ –ionization slope ($d(f_{EWcorot})/d(eV)$) and the major and minor axes systems’ metallicity (Figure 9). Figure 10 shows only systems residing along the galaxies’ major axis (within 20 degrees) and their $d(f_{EWcorot})/d(eV)$ as a function of CGM metallicity. The upper left panel shows the systems with detected C II absorption and the data points are colour-coded based on its $f_{EWcorot}$. The upper right panel shows the same but for Si II. Although the sample is small, we find that for low ionization gas (both C II and Si II), the lowest metallicity gas has the highest co-rotation fraction. The absorbers with the lowest metallicities also have negative $d(f_{EWcorot})/d(eV)$, which indicates cooler, less ionized gas has a higher consistency with a co-rotation model than the higher ionization gas. On the contrary, absorption systems with only a small fraction of absorption consistent with co-rotation have higher metallicities and $d(f_{EWcorot})/d(eV)$ that are consistent with being positive. It would seem like both metallicity and co-rotation fraction could be an effective way of identifying cosmological accretion onto galaxies. The bottom panels of Figure 10 are the same as the top but for Si III and O VI absorption. While we find that both Si III and O VI have high EW co-rotation fractions at low metallicities, they also have high EW co-rotation fractions for the highest metallicity systems, which is not seen in the lower phase.

Overall these results are intriguing and could be suggestive of two forms of accretion. The low ionization gas that is co-rotating strongly with the galaxy has the lowest metallicity, which could arise from accretion along cosmological filaments containing metal-poor gas that is driving the angular momentum of their galaxies. The signature of co-rotation is also seen in the higher ionization phases also predicted by simulations (Oppenheimer 2018; Stern et al. 2023; Hafen et al. 2022), which indicates that it is a multiphase accretion. On the other hand, the higher ionization lines also show high co-rotation fractions ($f_{EWcorot} > 0.5$) for the highest metallicity systems in our sample. It is unlikely that this is the edge of the filaments or a higher ionization sheath that surrounds the filaments given the higher metallicity. One possibility is that this gas is recycled material that is cooling and joining with the accretion along the major axis. This is consistent with cosmological simulations predictions of hot gas ($T \sim 10^6$ K) that accretes through the CGM and cools as it joins the extended plane of the disk (Stern et al. 2023). Using FIRE simulations, Hafen et al. (2022) predicted that the rotating cooling gas is the dominant source of accretion onto Milky-Way mass galaxies. However, the hot gas at virial temperature decelerates with a rotation pattern and then starts to cool down and accretes onto the disk. Thus, we could be observing two different phases of gas accretion. This may also be indicative of fountain accretion (Fraternali 2017) at larger scales and distances from the disk. As the feedback materials with higher metallicity travel through the halo and mix with the hot

CGM, it triggers and accelerates the cooling of hot gas which leads to the accretion of gas from the hot phase of CGM.

Figure 11 presents $d(f_{\text{EWcorot}})/d(\text{eV})$ as a function of CGM metallicity for systems observed along the minor axis of galaxies ($\Phi \geq 60$ degree). While we have even fewer data, and fewer ions, along the galaxy minor axis, we still find it interesting to discuss and hope to expand on the sample in future studies. The top panel shows the systems with detected Si III absorption and the data points are colour-coded based on its f_{EWcorot} . The bottom panel show the same but for O VI absorption. We find that minor axis absorbers, mostly have negative $d(f_{\text{EWcorot}})/d(\text{eV})$ values and exhibit higher metallicities, which is true for both low-ionization Si III absorption and high-ionization O VI. This is the opposite trend compare to major axis systems presented in Figure 10, where systems with smaller $d(f_{\text{EWcorot}})/d(\text{eV})$ and higher EW co-rotation fraction are associated with the highest metallicities. This could be explained as outflowing material that is still kinematically coupled to the host galaxy. This is consistent with *GasFlows-I*, where we surprisingly found the signatures of co-rotation in H I absorption along the minor axis within the virial radius of galaxies. Whereas, systems with smaller $d(f_{\text{EWcorot}})/d(\text{eV})$ and low EW co-rotation fraction could be explained as recycled gas that is flowing back onto the galaxy.

Regardless of the underlying spatial, kinematic, and ionization structure of the CGM inferred in this discussion, the co-rotation fractions provide stringent constraints on simulations. They have proven to be a valuable quantifier for characterizing the azimuthal, metallicity, and kinematic relationships of the CGM, challenging simulators and inviting them to adopt these quantifiers.

5 CONCLUSION

We used the EW co-rotation fraction (f_{EWcorot}) method that we developed in *GasFlows-I* to study the kinematic connection between the multiphase CGM absorption and host galaxy rotation. Here we examined 27 galaxy–CGM pairs with galaxies span over a redshift range of 0.09–0.5. When possible, we use the CGM metal absorption lines C II $\lambda 1334$, C III $\lambda 977$, C IV $\lambda 1548$, Si II $\lambda 1260$, Si III $\lambda 1206$, Si IV $\lambda 1393$, N II $\lambda 1083$, N III $\lambda 989$, N V $\lambda 1238$, Mg II $\lambda 2796$, and O VI $\lambda 1031$, to study the f_{EWcorot} for different ions. The absorption lines are detected in the spectra of background quasars ($D = 21 - 276$ kpc) observed with *HST/COS* and Keck/HIRES or VLT/UVES. The galaxies have a halo mass range of $\log(M_{\text{h}}/M_{\odot}) = 10.5 - 12.3$ and their rotation curves were obtained with Keck/ESI as part of the analysis in *GasFlows-I*. We investigate the dependence of f_{EWcorot} on H I column density ($\log(N(\text{H I})/\text{cm}^{-2})$), impact parameter normalised to the virial radius, and azimuthal angle. We examine the change in the EW co-rotation fraction as a function of ionization potential ($d(f_{\text{EWcorot}})/d(\text{eV})$) and also explore any connection between the distribution of $d(f_{\text{EWcorot}})/d(\text{eV})$ as a function of galaxy and gas properties. We summarise our results as follows:

(i) The median EW co-rotation fractions for all the ions are consistent within the errors with Si II: 0.5 ± 0.4 , C II: 0.8 ± 0.3 , Si III: 0.5 ± 0.3 , C III: 0.7 ± 0.3 and O VI: 0.6 ± 0.3 . Thus, for a general population of absorbers, our results suggest that all ions appear to have similar amounts of co-rotation.

(ii) We find that the EW co-rotation fraction of lower- and higher ionization potential species are likely increasing with $\log(N(\text{H I})/\text{cm}^{-2})$. This correlation is likely shallower for higher ionization gas.

(iii) The f_{EWcorot} of C II, Si II, Si III and C III decreases with increasing D/R_{vir} while the O VI co-rotation is more constant across

the full range of D/R_{vir} , which is similar to H I, and H I could be flatter since it traces both low and high ions.

(iv) The average f_{EWcorot} of all the ions is consistent with almost being flat across all Φ bins within the errors, however there is a possible peak at intermediate azimuthal angles. We do not find a significant variation between different ions in each Φ bin.

(v) The larger number of O VI detections enabled us to investigate where the majority of co-rotating gas is found. Highly co-rotating O VI primarily resides along the galaxies' major axis. This differs from the results in *GasFlows-I*, where they showed a bimodal distribution of co-rotating H I systems within the CGM with respect to azimuthal angles.

(vi) We examine the change in the EW co-rotation fraction as a function of ionization potential ($d(f_{\text{EWcorot}})/d(\text{eV})$) for individual systems. We find that on average, the co-rotation fraction decreases with increasing ionization potential. Our results demonstrate that the low-ionization CGM has a higher co-rotation fraction compared to the high-ionization CGM.

(vii) Our results suggest a dependence of $d(f_{\text{EWcorot}})/d(\text{eV})$ on CGM metallicity. It appears that within 20 degrees of the galaxies' major axes ($\Phi < 20$), systems with smaller $d(f_{\text{EWcorot}})/d(\text{eV})$ have lower metallicities and high co-rotation fractions (consistent with cosmic filament accretion), whereas systems with larger slopes exhibit higher metallicities and high co-rotation fractions (which could be recycled gas being accreted). On the other hand, along the minor axis ($\Phi \geq 60$), absorbers have negative $d(f_{\text{EWcorot}})/d(\text{eV})$ with higher metallicities consistent with outflows (for those having high co-rotation fraction) or recycled gas (for those having lower co-rotation fractions).

In this work, for the first time, we investigate how the kinematics of the multiphase CGM absorption relates to galaxy rotation. Our results imply a significant amount of gas that is consistent with co-rotation in both low- and high- ionization CGM. By examining the change in co-rotation as a function of ionization potential, we demonstrated that the low-ionization phase is more kinematically consistent with the host galaxy rotation and thus an accretion scenario. The evidence of co-rotation that we found in high-ionization gas could imply the hot CGM accretion. While there is a lot to be learnt from examining single ions and their connections to galaxies, as we have shown here, having a large range of ions allows us to reveal the underlying relationship between galaxies and their multiphase gas flows. While we find evidence for a relationship between the spatial distribution of the gas, its kinematics, and metallicities, we require additional data to fully quantify how gas accretion, both for low and high ionization metal lines, occurs onto galaxies.

ACKNOWLEDGEMENTS

The authors thank the referee for insightful comments that have improved the manuscript. H.N, G.G.K, and N.M.N. acknowledge the support of the Australian Research Council Centre of Excellence for All Sky Astrophysics in 3 Dimensions (ASTRO 3D), through project number CE170100013. M.T.M acknowledges the support of the Australian Research Council through Future Fellowship grant FT180100194. Some of the data presented herein were obtained at the W. M. Keck Observatory, which is operated as a scientific partnership among the California Institute of Technology, the University of California and the National Aeronautics and Space Administration. The Observatory was made possible by the generous financial support of the W. M. Keck Foundation. Observations were supported by Swinburne Keck programs with

2010A_W007E, 2010B_W032E, 2014A_W178E, 2014B_W018E, 2015_W187E, and 2016A_W056E. The authors wish to recognise and acknowledge the very significant cultural role and reverence that the summit of Maunakea has always had within the indigenous Hawaiian community. We are most fortunate to have the opportunity to conduct observations from this mountain.

DATA AVAILABILITY

The data underlying this paper will be shared following mutually agreeable arrangements with the corresponding authors.

REFERENCES

- Afruni A., Pezzulli G., Fraternali F., Grønnow A., 2023, *MNRAS*, **524**, 2351
- Anglés-Alcázar D., Faucher-Giguère C.-A., Kereš D., Hopkins P. F., Quataert E., Murray N., 2017, *MNRAS*, **470**, 4698
- Barcons X., Lanzetta K. M., Webb J. K., 1995, *Nature*, **376**, 321
- Bell E. F., McIntosh D. H., Katz N., Weinberg M. D., 2003, *ApJS*, **149**, 289
- Bordoloi R., et al., 2011, *ApJ*, **743**, 10
- Bouché N., Hohensee W., Vargas R., Kacprzak G. G., Martin C. L., Cooke J., Churchill C. W., 2012, *MNRAS*, **426**, 801
- Bouché N., Murphy M. T., Kacprzak G. G., Péroux C., Contini T., Martin C. L., Dessauges-Zavadsky M., 2013, *Science*, **341**, 50
- Bouché N., et al., 2016, *ApJ*, **820**, 121
- Bryan G. L., Norman M. L., 1998, *ApJ*, **495**, 80
- Chambers K. C., et al., 2016, arXiv e-prints, p. arXiv:1612.05560
- Chen H.-W., Helsby J. E., Gauthier J.-R., Shectman S. A., Thompson I. B., Tinker J. L., 2010, *ApJ*, **714**, 1521
- Churchill C. W., Nielsen N. M., Kacprzak G. G., Trujillo-Gomez S., 2013, *ApJ*, **763**, L42
- Churchill C. W., Vander Vliet J. R., Trujillo-Gomez S., Kacprzak G. G., Klypin A., 2015, *ApJ*, **802**, 10
- Côté S., Wyse R. F. G., Carignan C., Freeman K. C., Broadhurst T., 2005, *ApJ*, **618**, 178
- Crighton N. H. M., Hennawi J. F., Prochaska J. X., 2013, *ApJ*, **776**, L18
- Danovich M., Dekel A., Hahn O., Ceverino D., Primack J., 2015, *MNRAS*, **449**, 2087
- Dekel A., Birnboim Y., 2006, *MNRAS*, **368**, 2
- Dekel A., et al., 2009, *Nature*, **457**, 451
- Dekker H., D’Odorico S., Kaufer A., Delabre B., Kotzlowski H., 2000, in Iye M., Moorwood A. F., eds, *Society of Photo-Optical Instrumentation Engineers (SPIE) Conference Series Vol. 4008*, Proc. SPIE. pp 534–545, doi:10.1117/12.395512
- Diamond-Stanic A. M., Coil A. L., Moustakas J., Tremonti C. A., Sell P. H., Mendez A. J., Hickox R. C., Rudnick G. H., 2016, *ApJ*, **824**, 24
- Dutta R., Srianand R., Gupta N., Momjian E., Noterdaeme P., Petitjean P., Rahmani H., 2017, *MNRAS*, **465**, 588
- Faucher-Giguère C.-A., Kereš D., 2011a, *MNRAS*, **412**, L118
- Faucher-Giguère C.-A., Kereš D., 2011b, *MNRAS*, **412**, L118
- Faucher-Giguère C.-A., Hopkins P. F., Kereš D., Muratov A. L., Quataert E., Murray N., 2015, *MNRAS*, **449**, 987
- Ferland G. J., et al., 2013, *Rev. Mex. Astron. Astrofis.*, **49**, 137
- Fielding D., Quataert E., McCourt M., Thompson T. A., 2017, *MNRAS*, **466**, 3810
- Ford A. B., Davé R., Oppenheimer B. D., Katz N., Kollmeier J. A., Thompson R., Weinberg D. H., 2014, *MNRAS*, **444**, 1260
- Ford A. B., et al., 2016, *MNRAS*, **459**, 1745
- Fraternali F., 2017, in Fox A., Davé R., eds, *Astrophysics and Space Science Library Vol. 430*, Gas Accretion onto Galaxies. p. 323 (arXiv:1612.00477), doi:10.1007/978-3-319-52512-9_14
- French D. M., Wakker B. P., 2020, *ApJ*, **897**, 151
- Fumagalli M., Prochaska J. X., Kasen D., Dekel A., Ceverino D., Primack J. R., 2011, *MNRAS*, **418**, 1796
- Girelli G., Pozzetti L., Bolzonella M., Giocoli C., Marulli F., Baldi M., 2020, *A&A*, **634**, A135
- Haardt F., Madau P., 1996, *ApJ*, **461**, 20
- Hafen Z., et al., 2017, *MNRAS*, **469**, 2292
- Hafen Z., et al., 2022, *MNRAS*, **514**, 5056
- Ho S. H., Martin C. L., Kacprzak G. G., Churchill C. W., 2017, *ApJ*, **835**, 267
- Ho S. H., Martin C. L., Turner M. L., 2019, *ApJ*, **875**, 54
- Kacprzak G. G., Churchill C. W., Steidel C. C., Murphy M. T., 2008, *AJ*, **135**, 922
- Kacprzak G. G., Churchill C. W., Ceverino D., Steidel C. C., Klypin A., Murphy M. T., 2010, *ApJ*, **711**, 533
- Kacprzak G. G., Churchill C. W., Evans J. L., Murphy M. T., Steidel C. C., 2011, *Monthly Notices of the Royal Astronomical Society*, **416**, 3118
- Kacprzak G. G., Churchill C. W., Nielsen N. M., 2012, *The Astrophysical Journal*, **760**, L7
- Kacprzak G. G., et al., 2014, *ApJ*, **792**, L12
- Kacprzak G. G., Muzahid S., Churchill C. W., Nielsen N. M., Charlton J. C., 2015, *ApJ*, **815**, 22
- Kacprzak G. G., et al., 2019a, *ApJ*, **870**, 137
- Kacprzak G. G., Pointon S. K., Nielsen N. M., Churchill C. W., Muzahid S., Charlton J. C., 2019b, *ApJ*, **886**, 91
- Kacprzak G. G., Nielsen N. M., Nateghi H., Churchill C. W., Pointon S. K., Nanayakkara T., Muzahid S., Charlton J. C., 2021, *MNRAS*, **500**, 2289
- Kato T., Omachi S., Aso H., 2002, in Caelli T., Amin A., Duin R. P. W., de Ridder D., Kamel M., eds, *Structural, Syntactic, and Statistical Pattern Recognition*. Springer Berlin Heidelberg, Berlin, Heidelberg, pp 405–413
- Katz N., Keres D., Dave R., Weinberg D. H., 2003, in Rosenberg J. L., Putman M. E., eds, *Astrophysics and Space Science Library Vol. 281*, The IGM/Galaxy Connection. The Distribution of Baryons at z=0. p. 185 (arXiv:astro-ph/0209279), doi:10.1007/978-94-010-0115-1_34
- Kereš D., Katz N., Weinberg D. H., Davé R., 2005, *MNRAS*, **363**, 2
- Kereš D., Katz N., Fardal M., Davé R., Weinberg D. H., 2009, *MNRAS*, **395**, 160
- Klimenko V. V., Kulkarni V., Wake D. A., Poudel S., Bershady M. A., Péroux C., Lundgren B., 2023, *ApJ*, **954**, 115
- Lan T.-W., Mo H., 2018, *ApJ*, **866**, 36
- Lan T.-W., Ménard B., Zhu G., 2014, *ApJ*, **795**, 31
- Lopez S., et al., 2020, *MNRAS*, **491**, 4442
- Lundgren B. F., et al., 2021, *ApJ*, **913**, 50
- Martin D. C., et al., 2019a, *Nature Astronomy*, **3**, 822
- Martin C. L., Ho S. H., Kacprzak G. G., Churchill C. W., 2019b, *ApJ*, **878**, 84
- Morris S. L., Weymann R. J., Dressler A., McCarthy P. J., Smith B. A., Terrielle R. J., Giovanelli R., Irwin M., 1993, *ApJ*, **419**, 524
- Murphy M. T., Kacprzak G. G., Savognan G. A. D., Carswell R. F., 2019, *MNRAS*, **482**, 3458
- Muzahid S., Kacprzak G. G., Churchill C. W., Charlton J. C., Nielsen N. M., Mathes N. L., Trujillo-Gomez S., 2015, *ApJ*, **811**, 132
- Nateghi H., Kacprzak G. G., Nielsen N. M., Muzahid S., Churchill C. W., Pointon S. K., Charlton J. C., 2021, *MNRAS*, **500**, 3987
- Nateghi H., Kacprzak G. G., Nielsen N. M., Murphy M. T., Churchill C. W., Muzahid S., Sameer Charlton J. C., 2024, *MNRAS*, **533**, 1321
- Nelson D., Genel S., Pillepich A., Vogelsberger M., Springel V., Hernquist L., 2016, *MNRAS*, **460**, 2881
- Nelson D., et al., 2019, *MNRAS*, **490**, 3234
- Nestor D. B., Johnson B. D., Wild V., Ménard B., Turnshek D. A., Rao S., Pettini M., 2011, *MNRAS*, **412**, 1559
- Ng M., Nielsen N. M., Kacprzak G. G., Pointon S. K., Muzahid S., Churchill C. W., Charlton J. C., 2019, *ApJ*, **886**, 66
- Nielsen N. M., Churchill C. W., Kacprzak G. G., Murphy M. T., 2013, *ApJ*, **776**, 114
- Nielsen N. M., Kacprzak G. G., Muzahid S., Churchill C. W., Murphy M. T., Charlton J. C., 2017, *The Astrophysical Journal*, **834**, 148
- Nielsen N. M., Kacprzak G. G., Pointon S. K., Murphy M. T., Churchill C. W., Davé R., 2020, arXiv e-prints, p. arXiv:2002.08516
- Oppenheimer B. D., 2018, *MNRAS*, **480**, 2963
- Péroux C., et al., 2016, *MNRAS*, **457**, 903

Péroux C., et al., 2019, *MNRAS*, **485**, 1595
 Péroux C., Nelson D., van de Voort F., Pillepich A., Marinacci F., Vogelsberger M., Hernquist L., 2020, *MNRAS*, **499**, 2462
 Pointon S. K., Kacprzak G. G., Nielsen N. M., Muzahid S., Murphy M. T., Churchill C. W., Charlton J. C., 2019, *ApJ*, **883**, 78
 Rahmani H., et al., 2018, *MNRAS*, **474**, 254
 Rudie G. C., et al., 2012, *ApJ*, **750**, 67
 Sameer et al., 2021, *MNRAS*, **501**, 2112
 Sameer et al., 2022, *MNRAS*, **510**, 5796
 Sameer et al., 2024, *MNRAS*,
 Schroetter I., et al., 2019, *MNRAS*, **490**, 4368
 Sheinis A. I., Bolte M., Epps H. W., Kibrick R. I., Miller J. S., Radovan M. V., Bigelow B. C., Sutin B. M., 2002, *PASP*, **114**, 851
 Simard L., et al., 2002, *The Astrophysical Journal Supplement Series*, **142**, 1
 Steidel C. C., Dickinson M., Persson S. E., 1994, *ApJ*, **437**, L75
 Steidel C. C., Kollmeier J. A., Shapley A. E., Churchill C. W., Dickinson M., Pettini M., 2002, *ApJ*, **570**, 526
 Steidel C. C., Erb D. K., Shapley A. E., Pettini M., Reddy N., Bogosavljević M., Rudie G. C., Rakic O., 2010, *ApJ*, **717**, 289
 Stern J., Fielding D., Hafen Z., Su K.-Y., Naor N., Faucher-Giguère C.-A., Quataert E., Bullock J., 2023, *arXiv e-prints*, p. [arXiv:2306.00092](https://arxiv.org/abs/2306.00092)
 Stewart K. R., 2017, *Gas Accretion and Angular Momentum*. p. 249, [doi:10.1007/978-3-319-52512-9_11](https://doi.org/10.1007/978-3-319-52512-9_11)
 Stewart K. R., Kaufmann T., Bullock J. S., Barton E. J., Maller A. H., Diemand J., Wadsley J., 2011a, *ApJ*, **735**, L1
 Stewart K. R., Kaufmann T., Bullock J. S., Barton E. J., Maller A. H., Diemand J., Wadsley J., 2011b, *ApJ*, **738**, 39
 Stewart K. R., Brooks A. M., Bullock J. S., Maller A. H., Diemand J., Wadsley J., Moustakas L. A., 2013, *ApJ*, **769**, 74
 Stewart K. R., et al., 2017, *ApJ*, **843**, 47
 Stocke J. T., Keeney B. A., Danforth C. W., Shull J. M., Froning C. S., Green J. C., Penton S. V., Savage B. D., 2013, *ApJ*, **763**, 148
 Strawn C., et al., 2021, *MNRAS*, **501**, 4948
 Suresh J., Nelson D., Genel S., Rubin K. H. R., Hernquist L., 2019, *MNRAS*, **483**, 4040
 Tripp T. M., Lu L., Savage B. D., 1998, *The Astrophysical Journal*, **508**, 200
 Tripp T. M., Sembach K. R., Bowen D. V., Savage B. D., Jenkins E. B., Lehner N., Richter P., 2008, *ApJS*, **177**, 39
 Tumlinson J., et al., 2011, *Science*, **334**, 948
 Tumlinson J., Peebles M. S., Werk J. K., 2017, *ARA&A*, **55**, 389
 Vogt N. P., Forbes D. A., Phillips A. C., Gronwall C., Faber S. M., Illingworth G. D., Koo D. C., 1996, *ApJ*, **465**, L15
 Wakker B. P., Hernandez A. K., French D. M., Kim T.-S., Oppenheimer B. D., Savage B. D., 2015, *ApJ*, **814**, 40
 Weiner B. J., et al., 2009, *ApJ*, **692**, 187
 Wendt M., Bouché N. F., Zabl J., Schroetter I., Muzahid S., 2021, *MNRAS*, **502**, 3733
 Weng S., Péroux C., Ramesh R., Nelson D., Sadler E. M., Zwaan M., Bollo V., Casavecchia B., 2023, *arXiv e-prints*, p. [arXiv:2310.18310](https://arxiv.org/abs/2310.18310)
 Werk J. K., Prochaska J. X., Thom C., Tumlinson J., Tripp T. M., O'Meara J. M., Peebles M. S., 2013, *ApJS*, **204**, 17
 Werk J. K., et al., 2014, *ApJ*, **792**, 8
 Werk J. K., et al., 2016, *ApJ*, **833**, 54
 Zabl J., et al., 2019, *MNRAS*, **485**, 1961
 Zibetti S., Ménard B., Nestor D. B., Quider A. M., Rao S. M., Turnshek D. A., 2007, *ApJ*, **658**, 161
 van de Voort F., Schaye J., 2012, *MNRAS*, **423**, 2991
 van de Voort F., Schaye J., Booth C. M., Haas M. R., Dalla Vecchia C., 2011, *MNRAS*, **414**, 2458
 van de Voort F., Schaye J., Altay G., Theuns T., 2012, *MNRAS*, **421**, 2809

coordinates and redshift (z_{gal}), impact parameter (D) and virial radius normalised impact parameter (D/R_{vir}), galaxy inclination angle (i), the azimuthal angle (Φ), neutral hydrogen column density ($\log(N(\text{H I})/\text{cm}^{-2})$) and halo mass ($\log(M_{\text{h}}/M_{\odot})$).

APPENDIX A: GALAXY-CGM ABSORPTION OBSERVATION

Details of each galaxy-absorption pairs are provided in Table A1. The table presents the background quasar field, galaxy ID, galaxy

Table A1. Galaxy–absorption observations.

Quasar	Galaxy	RA _{gal}	DEC _{gal}	z _{gal}	D (kpc)	D/R _{vir}	i (deg)	Φ (deg)	log(N(HI)/cm ⁻²)	log(M _h /M _⊙)	g - r
J035128-142908	J0351G1	03:51:27.87	-14:28:57.9	0.356992	72.3±0.4	0.53 ^{+0.07} _{-0.07}	28.5 ^{+19.8} _{-12.5}	4.9 ^{+3.3} _{-4.9}	16.86 ± 0.03	11.55 ^{+0.1} _{-0.1}	0.29
J040748-121136	J0407G1	04:07:49.67	-12:11:05.5	0.495164	107.6±0.4	0.78 ^{+0.07} _{-0.07}	67.2 ^{+7.6} _{-7.5}	21.0 ^{+5.3} _{-3.7}	14.34 ± 0.56	11.54 ^{+0.1} _{-0.1}	0.45 ^a
J045608-215909	J0456G1	04:56:08.93	-21:59:29.2	0.381511	103.4±0.3	0.6 ^{+0.1} _{-0.07}	57.1 ^{+19.9} _{-2.4}	63.8 ^{+4.3} _{-2.7}	15.1 ± 0.39	11.86 ^{+0.12} _{-0.1}	0.45 ^a
J045608-215909	J0456G2	04:56:09.69	-21:59:03.9	0.277938	50.7±0.4	0.4 ^{+0.07} _{-0.07}	71.2 ^{+2.2} _{-2.6}	78.4 ^{+2.1} _{-2.04}	14.78 ± 0.22	11.49 ^{+0.1} _{-0.1}	0.45 ^a
J085334+434902	J0853G2	08:53:45.24	+43:51:08.2	0.163403	26.2±0.1	0.18 ^{+0.07} _{-0.07}	70.1 ^{+1.4} _{-0.8}	56.0 ^{+0.8} _{-0.8}	19.93 ± 0.01	11.7 ^{+0.1} _{-0.09}	0.45 ^a
J091440+282330	J0914G1	09:14:41.76	+28:23:51.2	0.244312	105.9±0.1	0.81 ^{+0.07} _{-0.07}	39.0 ^{+0.4} _{-0.2}	18.2 ^{+1.1} _{-1.0}	15.55 ± 0.03	11.54 ^{+0.1} _{-0.1}	0.17
J094331+053131	J0943G1	09:43:30.72	+05:31:17.5	0.353052	96.5±0.3	0.78 ^{+0.07} _{-0.07}	44.4 ^{+1.2} _{-1.2}	8.2 ^{+3.0} _{-5.0}	16.46 ± 0.03	11.44 ^{+0.1} _{-0.1}	0.29
J095000+483129	J0950G1	09:50:01.01	+48:31:02.3	0.211866	93.6±0.2	0.43 ^{+0.2} _{-0.12}	47.7 ^{+0.1} _{-0.1}	16.6 ^{+0.1} _{-0.1}	18.48 ± 0.19	12.22 ^{+0.24} _{-0.17}	0.45 ^a
PG1001+291	PG1001G1	10:04:02.37	+28:55:12.3	0.137403	56.7±0.2	0.93 ^{+0.06} _{-0.07}	79.1 ^{+2.2} _{-2.1}	12.4 ^{+2.4} _{-2.9}	14.98 ± 0.03	10.59 ^{+0.08} _{-0.1}	0.20
J100902+071343	J1009G1	10:09:02.74	+07:13:37.7	0.227855	64.0±0.8	0.44 ^{+0.08} _{-0.07}	66.3 ^{+0.6} _{-0.9}	89.6 ^{+0.4} _{-1.3}	17.23 ± 0.16	11.68 ^{+0.1} _{-0.09}	0.45 ^a
J104116+061016	J1041G1	10:41:06.32	+06:09:13.5	0.442173	56.2±0.3	0.3 ^{+0.1} _{-0.08}	49.8 ^{+7.4} _{-5.2}	4.3 ^{+0.9} _{-1.0}	18.19 ± 0.14	11.94 ^{+0.14} _{-0.11}	0.45 ^a
PG1116+215	PG1116G1	11:19:06.70	+21:18:28.8	0.138114	138.0±0.2	0.76 ^{+0.1} _{-0.09}	26.3 ^{+0.8} _{-0.4}	34.4 ^{+0.4} _{-0.4}	16.2 ± 0.03	12.0 ^{+0.17} _{-0.13}	0.45 ^a
J113327+032719	J1133G1	11:33:28.27	+03:26:59.6	0.154598	55.6±0.1	0.52 ^{+0.06} _{-0.06}	23.5 ^{+0.4} _{-0.2}	56.1 ^{+1.7} _{-1.3}	16.76 ± 0.96	11.31 ^{+0.08} _{-0.08}	0.20
J113910-135043	J1139G2	11:39:09.52	-13:51:31.8	0.212259	174.8±0.1	0.98 ^{+0.1} _{-0.08}	85.0 ^{+0.1} _{-0.6}	80.4 ^{+0.4} _{-0.5}	15.33 ± 0.04	11.96 ^{+0.15} _{-0.11}	0.78
J113910-135043	J1139G3	11:39:10.01	-13:50:52.3	0.319255	73.3±0.4	0.47 ^{+0.08} _{-0.07}	83.4 ^{+1.4} _{-1.1}	39.1 ^{+1.9} _{-1.7}	16.19 ± 0.03	11.74 ^{+0.1} _{-0.1}	0.45 ^a
J113910-135043	J1139G4	11:39:11.53	-13:51:08.6	0.204194	93.2±0.3	0.61 ^{+0.08} _{-0.07}	81.6 ^{+0.4} _{-0.5}	5.8 ^{+0.4} _{-0.5}	16.28 ± 0.34	11.75 ^{+0.1} _{-0.1}	0.66
PG1216+069	PG1216G1	12:19:23.44	+06:38:20.1	0.123623	93.4±0.2	0.68 ^{+0.07} _{-0.07}	21.9 ^{+18.7} _{-21.8}	61.4 ^{+28.5} _{-13.4}	17.53 ± 1.47	11.64 ^{+0.1} _{-0.1}	0.41
J123304-003134	J1233G1	12:33:03.76	-00:31:59.6	0.318757	88.9±0.2	0.55 ^{+0.09} _{-0.07}	38.7 ^{+1.6} _{-1.8}	17.0 ^{+2.0} _{-2.3}	15.72 ± 0.02	11.78 ^{+0.11} _{-0.1}	0.45 ^a
J124154+572107	J1241G1	12:41:52.35	+57:20:53.6	0.205267	21.1±0.1	0.16 ^{+0.07} _{-0.07}	56.4 ^{+0.3} _{-0.3}	77.6 ^{+0.3} _{-0.4}	18.38 ± 0.16	11.55 ^{+0.1} _{-0.1}	0.45 ^a
J124154+572107	J1241G2	12:41:52.49	+57:20:42.6	0.217904	94.6±0.2	0.82 ^{+0.07} _{-0.07}	17.4 ^{+1.4} _{-1.6}	63.0 ^{+1.8} _{-2.1}	15.59 ± 0.12	11.38 ^{+0.1} _{-0.1}	0.29
J132222+464546	J1322G1	13:22:22.51	+46:45:46.0	0.214431	38.6±0.2	0.16 ^{+0.2} _{-0.14}	57.9 ^{+0.1} _{-0.2}	13.9 ^{+0.2} _{-0.2}	17.49 ± 0.2	12.32 ^{+0.29} _{-0.2}	0.69
J134251-005345	J1342G1	13:42:51.76	-00:53:49.3	0.227042	35.3±0.2	0.16 ^{+0.2} _{-0.13}	0.1 ^{+0.6} _{-0.0}	13.2 ^{+0.5} _{-0.4}	18.83 ± 0.05	12.26 ^{+0.26} _{-0.18}	0.45 ^a
J155504+362847	J1555G1	15:55:05.27	+36:28:48.1	0.189201	33.4±0.1	0.23 ^{+0.08} _{-0.07}	51.8 ^{+0.7} _{-0.7}	47.0 ^{+0.3} _{-0.8}	17.52 ± 0.22	11.69 ^{+0.1} _{-0.1}	0.32
J213135-120704	J2131G1	21:31:38.87	-12:06:44.1	0.4302	48.4±0.2	0.25 ^{+0.1} _{-0.1}	48.3 ^{+3.5} _{-3.7}	14.9 ⁺⁶ _{-4.9}	19.88 ± 0.1	11.99 ^{+0.16} _{-0.12}	0.45 ^a
J225357+160853	J2253G1	22:53:57.80	+16:09:05.5	0.153718	31.8±0.2	0.25 ^{+0.06} _{-0.06}	33.3 ^{+2.7} _{-2.0}	59.6 ^{+0.9} _{-1.8}	16.04 ± 0.73	11.52 ^{+0.1} _{-0.1}	0.45 ^a
J225357+160853	J2253G2	22:54:00.37	+16:09:06.4	0.352787	203.2±0.5	1.61 ^{+0.9} _{-0.07}	36.7 ^{+6.9} _{-4.6}	88.7 ^{+1.28} _{-4.8}	14.53 ± 0.05	11.46 ^{+0.1} _{-0.1}	0.08
J225357+160853	J2253G3	22:54:02.32	+16:09:33.4	0.390012	276.3±0.2	1.53 ^{+0.1} _{-0.08}	76.1 ^{+1.1} _{-1.2}	24.2 ^{+1.2} _{-1.2}	15.19 ± 0.04	11.92 ^{+0.14} _{-0.11}	0.45 ^a

^a For galaxies without observed $g - r$ colours, we assumed an Sbc-type spectrum based on the colours found for absorbing galaxies in previous studies (Steidel et al. 1994; Zibetti et al. 2007; Nielsen et al. 2013; Kacprzak et al. 2015).

APPENDIX B: CGM METAL ABSORPTION DETECTION

In Table B1, we provide the rest-frame equivalent width of detected absorbers within each galaxy's CGM, and their corresponding errors. In cases where absorption is not detected for a particular galaxy, we leave that entry empty, represented by three dots (\dots). The first column presents the host galaxy ID and columns two through twelve are ordered based on the ionization potential of the ions: Mg II λ 2796 (15.03 eV), Si II λ 1260 (16.3 eV), C II λ 1334 (24.4 eV), N II λ 1083 (29.6 eV), Si III λ 1206 (33.5 eV), Si IV λ 1393 (45.1 eV), N III λ 989 (47.5 eV), C III λ 977 (47.9 eV), C IV λ 1548 (64.5 eV), N V λ 1238 (97.9 eV), and O VI λ 1031 (138.1 eV).

APPENDIX C: EW CO-ROTATION FRACTION MEASUREMENTS

In Table C1, we provide the EW co-rotation fraction (f_{EWcorot}) for all the detected ions in each system, where typical uncertainties on f_{EWcorot} have a range of 0.001 – 0.006. The EW co-rotation fraction of H I is adopted from GasFlows-I. The last column presents the slope of the f_{EWcorot} vs. ionization with 1σ uncertainties ($d(f_{\text{EWcorot}})/d(\text{eV})$). Slopes are not reported for galaxies with fewer than three metal lines or where there is very little gas consistent with co-rotation.

This paper has been typeset from a $\text{\TeX}/\text{\LaTeX}$ file prepared by the author.

Table B1. Absorption EW and detection

Galaxy	$W_r(\text{Mg II})$	$W_r(\text{Si II})$	$W_r(\text{C II})$	$W_r(\text{N II})$	$W_r(\text{Si III})$	$W_r(\text{Si IV})$	$W_r(\text{N III})$	$W_r(\text{C III})$	$W_r(\text{C IV})$	$W_r(\text{N V})$	$W_r(\text{O VI})$
J0351G1	0.20 ± 0.04	0.13 ± 0.04	0.19 ± 0.04	...	0.44 ± 0.03	0.17 ± 0.04	0.62 ± 0.11	0.15 ± 0.03	0.38 ± 0.02
J0407G1	0.09 ± 0.0	0.22 ± 0.01
J0456G1	0.02 ± 0.01	...	0.11 ± 0.03	0.06 ± 0.0	0.21 ± 0.06	0.04 ± 0.03	0.21 ± 0.01
J0456G2	0.02 ± 0.02	0.28 ± 0.04	0.03 ± 0.02	...
J0853G2	...	0.29 ± 0.02	0.31 ± 0.01	0.14 ± 0.01	...	0.05 ± 0.07	0.09 ± 0.02	0.55 ± 0.02
J0914G1	...	0.03 ± 0.05	0.04 ± 0.04	...	0.09 ± 0.03	...	0.07 ± 0.03	0.34 ± 0.04
J0943G1	0.5 ± 0.05	...	0.12 ± 0.12	0.24 ± 0.06
J0950G1	0.65 ± 0.04	0.36 ± 0.05	0.41 ± 0.08	0.23 ± 0.02	0.52 ± 0.04	0.2 ± 0.09	0.24 ± 0.02	0.64 ± 0.02	0.11 ± 0.02
PG1001G1	0.11 ± 0.01
J1009G1	0.09 ± 0.01	0.08 ± 0.01	0.15 ± 0.01	...	0.26 ± 0.01	0.14 ± 0.02	0.16 ± 0.01	0.55 ± 0.04
J1041G1	0.68 ± 0.04	0.37 ± 0.04	0.48 ± 0.04	0.18 ± 0.03	0.53 ± 0.04	...	0.32 ± 0.02	0.57 ± 0.01	0.32 ± 0.03
PG1116G1	0.09 ± 0.01	0.05 ± 0.0	0.08 ± 0.01	0.03 ± 0.01	0.09 ± 0.01	0.02 ± 0.03	0.04 ± 0.0	0.11 ± 0.0	0.02 ± 0.02	...	0.07 ± 0.01
J1133G1	...	0.07 ± 0.05	0.09 ± 0.04	...	0.1 ± 0.04	0.04 ± 0.1	0.21 ± 0.04
J1139G2	0.03 ± 0.03	0.07 ± 0.01	0.04 ± 0.01
J1139G3	0.04 ± 0.03	0.31 ± 0.02	0.22 ± 0.02
J1139G4	0.11 ± 0.04	...	0.43 ± 0.05	...	0.09 ± 0.02	0.52 ± 0.02	0.24 ± 0.01
PG1216G1	0.09 ± 0.01	...	0.12 ± 0.04	0.59 ± 0.04	0.5 ± 0.02	0.09 ± 0.01	0.38 ± 0.08
J1233G1	0.05 ± 0.08	...	0.12 ± 0.05	0.47 ± 0.02	0.4 ± 0.03
J1241G1	1.0 ± 0.04	0.54 ± 0.04	0.63 ± 0.04	...	0.62 ± 0.03	0.52 ± 0.06	0.43 ± 0.02	0.65 ± 0.02	...	0.1 ± 0.03	0.5 ± 0.02
J1241G2	0.07 ± 0.02	0.25 ± 0.01	...	0.08 ± 0.03	0.36 ± 0.02
J1322G1	0.3 ± 0.04	0.23 ± 0.06	0.31 ± 0.1	...	0.58 ± 0.04	0.11 ± 0.07	0.17 ± 0.03	0.6 ± 0.02	0.35 ± 0.02
J1342G1	1.4 ± 0.04	0.71 ± 0.05	0.86 ± 0.05	0.46 ± 0.03	0.89 ± 0.04	0.24 ± 0.09	0.44 ± 6.6	1.1 ± 0.03	0.29 ± 0.03
J1555G1	0.31 ± 0.04	0.2 ± 0.05	0.31 ± 0.09	0.1 ± 0.05	0.43 ± 0.05	0.22 ± 0.07	0.24 ± 0.04	0.54 ± 0.03	0.31 ± 0.03
J2131G1	0.45 ± 0.04	0.26 ± 0.01	0.33 ± 0.02	0.16 ± 0.01	0.41 ± 0.03	0.5 ± 0.01	0.33 ± 0.09	...	0.31 ± 0.01
J2253G1	...	0.06 ± 0.02	0.14 ± 0.02	...	0.29 ± 0.05	0.21 ± 0.16	0.36 ± 0.06	...	0.18 ± 0.05
J2253G2	0.34 ± 0.03	...	0.07 ± 0.04	0.31 ± 0.05
J2253G3	...	0.02 ± 0.04	0.06 ± 0.04	...	0.04 ± 0.04	0.27 ± 0.03	...	0.04 ± 0.03	0.15 ± 0.04

Table C1. Absorption EW co-rotation fraction

Galaxy	EW co-rotation fraction ($f_{EWcorot}^a$)												$d(f_{EWcorot})/d(eV)[\times 10^{-4}]$
	H I	Mg II	Si II	C II	N II	Si III	Si IV	N III	C III	C IV	N V	O VI	
J0351G1	0.69	0.32	0.45	0.45	...	0.65	0.45	0.68	0.76	0.73	29.8 ± 8.9
J0407G1	0.57	0.72	0.6	... ^b
J0456G1	0.78	0.8	...	0.87	0.84	0.91	0.65	0.51	-30.1 ± 8.8
J0456G2	0.59	0.62	0.63	0.66	...	6.4 ± 2.4
J0853G2	0.57	...	0.97	0.95	0.97	...	0.97	0.97	0.9	-6.5 ± 9.9
J0914G1	0.23	...	0.23	0.14	...	0.19	...	0.07	0.16	-1.8 ± 7.1
J0943G1	0.93	0.99	...	0.97	0.97	-3.0 ± 1.0
J0950G1	0.29	0.04	0.1	0.09	0.05	0.16	0.06	0.07	0.21	0.1	2.4 ± 5.4
PG1001G1	0.64	0.98	... ^b
J1009G1	0.52	0.02	0.1	0.36	...	0.31	0.13	0.49	0.56	36.2 ± 10.9
J1041G1	0.94	1.0	1.0	1.0	1.0	1.0	...	1.0	0.99	0.99	-0.9 ± 0.2
PG1116G1	0.59	1.0	1.0	1.0	1.0	1.0	1.0	1.0	1.0	1.0	...	1.0	-0.2 ± 0.1
J1133G1	1.0	...	0.99	1.0	...	0.99	0.99	1.0	0.2 ± 0.4
J1139G2	0.03	0.01	0.01	0.02	... ^c
J1139G3	0.46	0.81	0.55	0.6	-11.4 ± 19.1
J1139G4	0.68	0.51	...	0.63	...	0.63	0.68	0.68	9.4 ± 7.0
PG1216G1	0.17	0.34	...	0.31	0.23	0.19	0.3	0.21	-7.0 ± 7.0
J1233G1	0.43	0.31	...	0.44	0.31	0.24	-10.6 ± 8.0
J1241G1	0.81	1.0	0.98	0.95	...	0.94	0.97	0.96	0.79	...	0.93	0.86	-8.4 ± 5.3
J1241G2	0.27	0.35	0.15	...	0.21	0.24	-4.2 ± 11.6
J1322G1	0.58	0.52	0.48	0.54	...	0.5	0.37	0.49	0.48	0.37	-11.4 ± 4.6
J1342G1	0.39	0.21	0.21	0.27	0.24	0.28	0.25	0.26	0.27	0.3	5.6 ± 2.2
J1555G1	0.64	0.92	0.83	0.85	0.83	0.87	0.91	0.91	0.82	0.76	-9.1 ± 4.0
J2131G1	0.58	0.97	0.95	0.93	0.94	0.83	0.76	0.94	...	0.66	-22.4 ± 6.6
J2253G1	0.45	...	0.31	0.42	...	0.3	0.27	0.33	...	0.29	-4.4 ± 5.7
J2253G2	0.74	0.96	...	0.8	0.67	-31.4 ± 0.4
J2253G3	0.01	...	0.0	0.0	...	0.0	0.0	...	0.0	0.0	... ^c

^a Typical uncertainties are on the order of 0.001 – 0.006 as determined from a bootstrap analysis where we varied the galaxy and absorption redshifts within their error bars.

^b Fewer than three metal lines were detected. A slope cannot be reliably measured.

^c No significant co-rotation was detected for this system.